CO adsorption on the oxygen overlayer continues to remove electron density from the surface, as occurs in Figure 1, causing the formation of predominantly bridge-bonded CO at high CO exposures (Figure 7e).

The postadsorption of oxygen (Figure 10) also suggests an electronic interaction. The adsorption of oxygen removes electron density from the molybdenum causing electron donation to the $\pi^*$ orbital of inclined carbon monoxide to decrease, resulting in bridged and terminal CO formation. Figure 10a shows a low CO coverage of $\theta_r = 0.28$ on an unmodified surface. If the effect of the oxygen were *only* steric, the addition of a small amount of oxygen (0.3 of saturation) (Figure 10b) should be accommodated in the many available open sites remaining, causing only a blue shift of the CO frequencies due to the presence of oxygen.[29] What is clearly seen, however, is the conversion of CO in an inclined bonding structure to a conventionally-bonded CO species.

## V. Conclusions

Four types of CO species with well-resolved, distinct $\nu$(CO) modes of 1130, 1345, ~1500, and 1920–2055 $cm^{-1}$ are observed on Mo(110), depending on the experimental conditions. The following is a summary of results obtained for the adsorption of CO on a clean and an oxygen-modified Mo(110) surface:

(1) At 120 K, CO molecules first occupy the 2-fold symmetric hollow sites on the Mo(110) surface in an inclined geometry; this CO species is characterized by a $\nu$(CO) mode of 1345 $cm^{-1}$. At higher CO coverages, the inclined species are converted to the conventionally-bonded CO species with frequencies in the range of 1920–2055 $cm^{-1}$, via an intermediate state with $\nu$(CO) at ~1500 $cm^{-1}$.

(2) For a CO/Mo(110) overlayer with only the inclined CO species, CO begins to dissociate on Mo(110) at ~200–250 K. An intermediate species to CO dissociation, Mo–C–O–Mo, with a $\nu$(CO) mode at 1130 $cm^{-1}$ is also observed. For a saturated CO/Mo(110) overlayer containing only the terminal CO, CO molecules both dissociate on and desorb unimolecularly from the Mo(110) surface upon heating.

(3) The dissociation of CO on Mo(110) can be hindered by a saturation coverage of preadsorbed oxygen. This effect is achieved by preventing the formation of the 1345-$cm^{-1}$ inclined-CO species. The postadsorption of $O_2$ on a CO/Mo(110) overlayer also indicates that oxygen induces the conversion of the 1345-$cm^{-1}$ CO species to the relatively unreactive conventionally-bonded CO, via an intermediate with a $\nu$(CO) of 1465–1535 $cm^{-1}$.

(4) The $\nu$(CO) vibrational frequencies of the CO species with various binding structures have provided direct vibrational evidence for reaction channels leading to CO dissociation and to inhibition of CO dissociation on the Mo(110) surface. These observations should provide significant insight into the interaction of CO with metal surfaces, especially with the relatively reactive early transition metal surfaces. In addition, the interconversion of various CO species on Mo(110) should provide a useful model system for future theoretical studies.

**Acknowledgment.** We gratefully acknowledge the financial support of this work by the Army Research Office. One of us (W.H.W.) also acknowledges the support of the National Science Foundation (Grant No. CHE-9003553).

**Registry No.** CO, 630-08-0; Mo, 7439-98-7.

(29) Xu, Z.; Surnev, L.; Uram, K. J.; Yates, J. T., Jr. To be submitted for publication.

# High-Energy Collisions of Fullerene Radical Cations with Target Gases: Capture of the Target Gas and Charge Stripping of $C_{60}^{\cdot+}$, $C_{70}^{\cdot+}$, and $C_{84}^{\cdot+}$

**Kenneth A. Caldwell, Daryl E. Giblin, and Michael L. Gross***

*Contribution from the Department of Chemistry, University of Nebraska at Lincoln, Lincoln, Nebraska 68588.* *Received August 28, 1991*

**Abstract:** This is a paper on the comprehensive study of the products formed when $C_{60}$ and $C_{70}$ radical cations undergo high-energy collisions with noble gases and with $D_2$, $N_2$, NO, or $O_2$. A new design four-sector tandem mass spectrometer was used to prove that, as a result of collisions, small target gases are incorporated into intact fullerene radical cations. For helium target gas, the endohedral complexes $C_{60}He^{\cdot+}$, $C_{70}He^{\cdot+}$, and $C_{84}He^{\cdot+}$ are produced directly from the radical cation precursor, and $C_{60}He_2^{\cdot+}$ is produced from $C_{70}^{\cdot+}$ colliding with He. The molecular gas $D_2$ also associates with $C_{60}^{\cdot+}$ in a high-energy collision. The kinetic energies for product ions resulting from capture of a target gas are derived and compared with experimental values to probe the mechanism of formation of the He-containing and $D_2$-containing fullerene product ions. The complex formed by capture of the He (or $D_2$) fragments to produce the majority of the lower mass product ions, both those that contain and those that do not contain the target gas. The internal energy of these complexes was varied by changing the center-of-mass collision energy, which is entirely converted to internal energy of the complex when the target gas is captured. More extensive fragmentation occurs when neon is used as a target gas, and Ne-containing product ions are also observed. Collisions of $C_{60}^{\cdot+}$ precursor ions with argon result in the formation of product ions corresponding formally to loss of odd-carbon fragments from $C_{60}Ar^{\cdot+}$ to produce, for example, $C_{55}Ar^{\cdot+}$. Collisions with the gases $N_2$, NO, and $O_2$ yield dramatically enhanced abundances of the doubly charged fullerene ions, thus facilitating the measurement of the second ionization energy by charge-stripping experiments. The work presented here builds on a preliminary communication[1] of these results.

## Introduction

The appealing structure proposed for $C_{60}$ has led to widespread scientific interest in this all-carbon molecule.[2] The novel, three-dimensional shape proposed by Kroto, Smalley, and coworkers is that of a truncated icosahedron, a highly symmetrical

* To whom correspondence should be addressed.

(1) Caldwell, K. A.; Giblin, D. E.; Hsu, C. S.; Cox, D.; Gross, M. L. *J. Am. Chem. Soc.* **1991**, *113*, 8519.

0002-7863/92/1514-3743$03.00/0 

hollow molecule comprised of 20 hexagons and 12 pentagons, with no two pentagons touching.[3,4] This structure is analogous to a soccer ball with C atoms at the vertices. There are 60 $\sigma$ and 30 $\pi$ bonds. All carbons are equivalent, and the strain energy resulting from nonplanar bonds is uniformly distributed over the sphere. This structure is supported by a large body of experimental data including X-ray crystallographic results.[5] The resulting structure is highly aromatic with 12 500 possible resonance structures.[6]

The proposed structure for $C_{70}$ resembles an American football. It is formed conceptually by splitting $C_{60}$ in half and placing a ring of 10 carbons between the halves.[4] It is believed that $C_{70}$ is the next closed, all-carbon molecule after $C_{60}$ in which the pentagons do not touch.[4,7] (For a drawing of $C_{60}$ and $C_{70}$, see refs 2, 4, 7, or 11.)

Early physical and chemical studies of $C_{60}$ were restricted to gas-phase species produced from a laser-vaporization, supersonic-expansion source.[3] In these studies, evidence for chemical inertness toward reaction with small molecules was presented for the first time,[8] and important physical properties were measured. For example, by using ultraviolet photoelectron spectroscopy of the negative ions, the HOMO–LUMO gap was measured for several fullerenes including $C_{50}$, $C_{60}$, and $C_{70}$, and comparison with the results for neighboring fullerenes led to the conclusion that these three fullerenes are closed-cage molecules.[9] The structural arguments made by Kroto[4] and Schmalz et al.[7] for assembly of large carbon cages by combination of pentagons and hexagons, which are the two most stable carbon ring structures found in polyaromatic hydrocarbons, also predict $C_{50}$, $C_{60}$, and $C_{70}$ to be closed-cage molecules.

Since the fall of 1990 when a method for producing bulk fullerenes was published,[10,11] UV–visible,[10-14] IR,[10-13,15,16] Raman,[16,17] and NMR[12,13,15,18-22] spectra of $C_{60}$ and to some extent of $C_{70}$ have been published. Nuclear magnetic resonance has played a major role in confirming the structure of $C_{60}$ and $C_{70}$. Perhaps the most convincing evidence for the presence of a $C_{60}$ molecule with $I_h$ symmetry and all equivalent carbons comes from $^{13}C$ NMR spectra, which show only a single resonance.[18] For $C_{70}$, the NMR spectra contain five peaks, and these have been assigned on the basis of the predicted structure which has $D_{5h}$ symmetry.[13,22]

Mass spectrometry and related methods have played a vital role in the discovery of fullerenes and more recently in the measurement of their properties. A value of 7.6 eV for the first ionization energy of $C_{60}$ was measured in two laboratories.[23,24] The measurement of the second ionization energy was also performed in several laboratories; however, some discrepancy exists in the results.[25-27] The rather large electron affinity of $C_{60}$ was established to be in the range of 2.6–2.8 eV.[9] A stable dianion was observed in both solution[15,20] and the gas phase.[28]

The ability to produce bulk quantities of the material has extended the number and kinds of mass spectrometric experiments that can be performed on $C_{60}$ and $C_{70}$. The requirement for a pulsed laser-vaporization ion source is removed, permitting the measurement of electron ionization (EI),[11-13,15,29] chemical ionization (CI),[15,30] and fast atom bombardment (FAB)[12,13] mass spectra of the crude extracts of the graphite soot or purified samples. These ionization sources produce a continuous beam of ions and permit collisional activation experiments to be performed separately on the molecular ions of $C_{60}$ and $C_{70}$ as well as of other fullerene species. Laser desorption mass spectra were also reported.[12,31]

Collisional activation spectra of $C_{60}$ and $C_{70}$ were reported by other researchers;[29,32,33] however, the resolution of the product ions is low owing to the use of a low-resolution electrostatic analyzer for MS2. A notable exception is the $C_{60}^{\bullet+}$ and $C_{70}^{\bullet+}$ four-sector tandem mass spectra reported by Schwarz and co-workers.[34a]

(2) For reviews, see: Curl, R. F.; Smalley, R. E. *Science* **1988**, *242*, 1017. Weltner, W., Jr.; van Zee, R. J. *Chem. Rev.* **1989**, *89*, 1713. Heath, J. R. *Spectroscopy* **1990**, *5*, 36. Stoddart, J. F. *Angew. Chem., Int. Ed. Engl.* **1991**, *30*, 70. Diederich, F.; Whetten, R. L. *Angew. Chem., Int. Ed. Engl.* **1991**, *30*, 678. Smalley, R. E. *Sciences (N.Y.)* **1991**, 22. Curl, R. F.; Smalley, R. E. *Sci. Am.* **1991**, *265* (4), 54.

(3) Kroto, H. W.; Heath, J. R.; O'Brien, S. C.; Curl, R. F.; Smalley, R. F. *Nature* **1985**, *318*, 162.

(4) Kroto, H. W. *Nature* **1987**, *329*, 529.

(5) Hawkins, J. M.; Meyer, A.; Lewis, T. A.; Loren, S.; Hollander, F. J. *Science* **1991**, *252*, 312. See also ref 11.

(6) Klein, D. J.; Schmalz, T. G.; Hite, G. E.; Seitz, W. A. *J. Am. Chem. Soc.* **1986**, *108*, 1301.

(7) Schmalz, T. G.; Seitz, W. A.; Klein, D. J.; Hite, G. E. *J. Am. Chem. Soc.* **1988**, *110*, 1113.

(8) (a) Zhang, Q. L.; O'Brien, S. C.; Heath, J. R.; Liu, Y.; Curl, R. F.; Kroto, H. W.; Smalley, R. E. *J. Phys. Chem.* **1986**, *90*, 525. See also: (b) McElvany, S. W.; Nelson, H. H.; Baronavski, A. P.; Watson, C. H.; Eyler, J. R. *Chem. Phys. Lett.* **1987**, *134*, 214.

(9) Yang, S. H.; Pettiette, C. L.; Conceicao, J.; Cheshnovsky, O.; Smalley, R. E. *Chem. Phys. Lett.* **1987**, *139*, 233. For a more recent determination of the electron affinity, see: Wang, L. S.; Conceicao, J.; Jin, C.; Smalley, R. E. *Chem. Phys. Lett.* **1991**, *179*, 449.

(10) Krätschmer, W.; Fostiropoulos, K.; Huffman, D. R. *Chem. Phys. Lett.* **1990**, *170*, 167.

(11) Krätschmer, W.; Lamb, L. D.; Fostiropoulos, K.; Huffman, D. R. *Nature* **1990**, *347*, 354.

(12) Ajie, H.; Alvarez, M. M.; Samir, J. A.; Rainer, D. B.; Diederich, F.; Fostiropoulos, K.; Huffman, D. R.; Krätschmer, W.; Rubin, Y.; Schriver, K. E.; Sensharma, D.; Whetten, R. L. *J. Phys. Chem.* **1990**, *94*, 8630.

(13) Taylor, R.; Hare, J. P.; Abdul-Sada, A. K.; Kroto, H. W. *J. Chem. Soc., Chem. Commun.* **1990**, *20*, 1423. The method of ionization used to produce the mass spectrum in Figure 1 of this paper is not mentioned, but we assume that it was electron ionization. At the end of the paper, FAB ionization results were discussed.

(14) Arbogast, J. W.; Darmanyan, A. P.; Foote, C. S.; Rubin, Y.; Diederich, F. N.; Alvarez, M. M.; Anz, S. J.; Whetten, R. L. *J. Phys. Chem.* **1991**, *95*, 11.

(15) Cox, D. M.; Behal, S.; Disko, M.; Gorun, S. M.; Greaney, M.; Hsu, C. S.; Kollin, E. B.; Millar, J.; Robbins, J.; Robbins, W.; Sherwood, R. D.; Tindall, P. *J. Am. Chem. Soc.* **1991**, *113*, 2940.

(16) Bethune, D. S.; Meijer, G.; Tang, W. C.; Rosen, H.; Golden, W. G.; Seki, H.; Brown, C. A.; de Vries, M. S. *Chem. Phys. Lett.* **1991**, *179*, 181.

(17) Bethune, D. S.; Meijer, G.; Tang, W. C.; Rosen, H. J. *Chem. Phys. Lett.* **1990**, *174*, 219.

(18) Johnson, R. D.; Meijer, G.; Bethune, D. S. *J. Am. Chem. Soc.* **1990**, *112*, 8983.

(19) Yannoni, C. S.; Johnson, R. D.; Meijer, G.; Bethune, D. S.; Salem, J. R. *J. Phys. Chem.* **1991**, *95*, 9. Tycko, R.; Haddon, R. C.; Dabbagh, G.; Glarum, S. H.; Douglass, D. C.; Mujsce, A. M. *J. Phys. Chem.* **1991**, *95*, 518. For a discussion of the effect of encapsulated atoms on the NMR chemical shift, see: Fowler, P. W.; Lazzeretti, P.; Zanasi, P. *Chem. Phys. Lett.* **1990**, *165*, 79.

(20) Bausch, J. W.; Prakash, G. K. S.; Olah, G. A. *J. Am. Chem. Soc.* **1991**, *113*, 3205.

(21) Yannoni, C. S.; Bernier, P. P.; Bethune, D. S.; Meijer, G.; Salem, J. R. *J. Am. Chem. Soc.* **1991**, *113*, 3190.

(22) Johnson, R. D.; Meijer, G.; Salem, J. R.; Bethune, D. S. *J. Am. Chem. Soc.* **1991**, *113*, 3619.

(23) Lichtenberger, D. L.; Nebesny, K. W.; Ray, C. D. *Chem. Phys. Lett.* **1991**, *176*, 203.

(24) Zimmerman, J. A.; Eyler, J. R.; Bach, S. B. H.; McElvany, S. W. *J. Chem. Phys.* **1991**, *94*, 3556.

(25) McElvany, S. W.; Ross, M. M.; Callahan, J. H. *Mater. Res. Soc. Symp. Proc.* **1990**, *206*, 697.

(26) Lifshitz, C.; Iraqi, M.; Peres, T. *Rapid Commun. Mass Spectrom.* **1991**, *5*, 238.

(27) This work.

(28) Limbach, P. A.; Schweikhard, L.; Cowen, K. A.; McDermott, M. T.; Marshall, A. G.; Coe, J. V. *J. Am. Chem. Soc.* **1991**, *113*, 6795.

(29) Luffer, D. R.; Schram, K. H. *Rapid Commun. Mass Spectrom.* **1990**, *4*, 552. Lifschitz, C.; Iraqi, M.; Peres, T.; Fischer, J. E. *Int. J. Mass Spectrom. Ion Processes* **1991**, *107*, 565.

(30) McElvany, S. W.; Callahan, J. H. *J. Phys. Chem.* **1991**, *95*, 6186. Ben-Amotz, D.; Cooks, R. G.; Dejarme, L.; Gunderson, J. C.; Hoke, S. H., II; Kahr, B.; Payne, G. L.; Wood, J. M. *Chem. Phys. Lett.* **1991**, *183*, 149. See also: Wood, J. M.; Kahr, B.; Hoke, S. H., II; Dejarme, L.; Cooks, R. G.; Ben-Amotz, D. *J. Am. Chem. Soc.* **1991**, *113*, 5907.

(31) Meijer, G.; Bethune, D. S. *Chem. Phys. Lett.* **1990**, *175*, 1. Ulmer, G.; Campbell, E. E. B.; Kuehnle, R.; Busmann, H. G.; Hertel, I. V. *Chem. Phys. Lett.* **1991**, *182*, 114.

(32) Young, A. B.; Cousins, L.; Harrision, A. G. *Rapid Commun. Mass Spectrom.* **1991**, *5*, 226.

(33) Doyle, R. J.; Ross, M. M. *J. Phys. Chem.* **1991**, *95*, 4954.

(34) (a) Weiske, T.; Bohme, D. K.; Hrusak, J.; Krätschmer, W.; Schwarz, H. *Angew. Chem., Int. Ed. Engl.* **1991**, *30*, 884. (b) Ross, M. M.; Callahan, J. H. *J. Phys. Chem.* **1991**, *95*, 5720.

They made the exciting discovery that the product ions formed as a result of high-energy collisions of $C_{60}^{\bullet+}$ or $C_{70}^{\bullet+}$ with He incorporate the He.

In this paper, we present the results of a comprehensive study of the product ions resulting from high-energy collisions of $C_{60}^{\bullet+}$ and $C_{70}^{\bullet+}$ with a variety of collision gases.[35] These studies were performed with both a three-sector and a four-sector mass spectrometer. An important feature of the four-sector instrument is the second-stage mass analyzer which allows product ions of widely differing kinetic energies to be transmitted and detected. During the course of this work, we became aware of the investigations of Schwarz and co-workers,[34a] in which a four-sector instrument was also used, and of Lifshitz and co-workers,[26] who used charge stripping to measure the second ionization energy of $C_{60}$ and $C_{70}$. Ross and Callahan[34b] then made the independent discovery that collisions of $C_{60}^{\bullet+}$ with He give $C_{60}He^{\bullet+}$, a species that was not reported by Schwarz and co-workers in their original paper.[34a] The results presented here corroborate and extend the results of those studies and of our earlier communication.[1]

## Experimental Section

**1. Materials.** The sample of $C_{60}$, which contained $C_{70}$ and $C_{84}$ in addition to higher mass fullerenes, was prepared by our collaborators and their colleagues at Exxon as previously described,[15] except that helium was used as the moderating gas. Collision gases He, Ne, Ar, Kr, Xe, $D_2$, $N_2$, NO, and $O_2$ were purchased from commercial suppliers and used as received.

**2. Mass Spectrometry.** Two instruments located at the University of Nebraska were used for these studies: a three-sector ($E_1BE_2$) mass spectrometer and a new prototype four-sector ($B_1E_1B_2E_2$) mass spectrometer, which is currently under evaluation. Both of these instruments were used to perform MS/MS experiments. In this experiment, a precursor ion with typically 8-keV kinetic energy was selected with the first stage of mass analysis and allowed to undergo collisions with a target gas. A spectrum of the ions produced from the precursor ion was obtained with a second stage of mass analysis. We refer to this spectrum of product ions as the collisionally activated dissociation (CAD) spectrum.

**a. Three-Sector Tandem Mass Spectrometry.** Initial MS/MS studies were performed on a Kratos MS50-TA. The precursor ion or "main beam" was selected with MS1 ($E_1B$), with a resolving power of 3000. An electrostatic analyzer (ESA) ($E_2$) comprises MS2.[36] Scanning the electric field of the second ESA from zero to above that required to transmit the main beam generates a mass-analyzed ion kinetic energy (MIKE) CAD spectrum. The kinetic energy scale was converted to a mass scale by using the relationship for conventional collisional activation given by eq 11 of this paper.

Fast atom bombardment (FAB) ionization (3-nitrobenzyl alcohol matrix, 6-keV Ar atoms) was first used for both normal and tandem mass spectrometric studies. However, the matrix background ions present at $m/z$ 720, which were codesorbed along with $C_{60}^{\bullet+}$, produced an interfering water loss ion at $m/z$ 702 in the CAD spectrum.

Matrix background ions were avoided by using electron ionization. The molecular ion currents were longer lived than those produced by a single loading of the sample on the FAB probe tip. An ionizing energy of 35 eV and a source temperature of 300 °C were used to produce singly and doubly charged molecular ions for MS/MS and charge-stripping experiments. For the initial experiments several microliters of the raw extract was placed in a glass capillary inserted into the tip of a standard Kratos heated solids probe. As the probe temperature approached 200 °C, hydrocarbon-like ions (deduced from the positive mass defect) were observed over a wide mass range. These ions disappear readily upon further heating the probe to 250–300 °C. Much more intense and longer lived ion beams were produced by a simple modification of the EI source performed while the source was removed from the instrument. A modified capillary containing the extract was placed into the channel of the source block that normally directs sample vapor from the heated solids probe into the interior of the source. The capillary was prevented from falling out by placing a small metal plate behind the capillary. The source was heated slowly until the sample was distilled into the electron beam. The modified capillary is a solid glass rod with a short, approximately 2-mm receptable at the tip; the length of the capillary is such that the tip extended slightly into the interior of the source.

**b. Translational Energy Loss Measurements.** Apparent second ionization energy measurements were made by using a procedure developed by others[37,38] and modified in this laboratory. Kinetic energy profiles were obtained for *both* the precursor ion or "main beam" and the doubly charged molecular ion produced from charge stripping, which appears at nominally $^1/_2$ the kinetic energy to charge ratio of the precursor ion. The kinetic energy of the doubly charged ion is nominally the same as that of the precursor ion, but the kinetic energy to charge ratio is $^1/_2$ that of the precursor ion; the precursor ions had a kinetic energy of 8 keV. To perform the charge-stripping experiment, the magnetic field, $B$, and the electric fields of $E_1$ and $E_2$ were set to transmit the 8-keV precursor ion to the detector located after $E_2$. At this point, $E_1$ and $E_2$ were linked to the accelerating potential via the potentials on the two electrodes that comprise each ESA. Because an ESA produces an electric field that disperses an ion according to its kinetic energy, the electric field of $E_1$, which was still linked to the accelerating potential, defined the kinetic energy of the precursor ions. Subsequently, $E_2$ was decoupled from $E_1$, and the electric field of the second ESA was scanned with a constant sweep width in parts per million about a selected value. At this point MS1, comprised of the first ESA and the magnet, served only to admit the precursor ion with defined kinetic energy to the collision cell located in the third field-free region after the magnet. The energy or $\beta$ slits located after $E_2$ were closed until the peak profile, as monitored during the scan of the electric field of $E_2$, was no longer flat-topped. The energy width of the source-produced ions was approximately 2.5 eV. The accelerating potential and the potentials of the electrodes of each ESA were controlled by a custom-built multiple-ion-detection system (MID). Essential features of the MID include the capability to specify the various potentials to high relative accuracy (within approximately 2 ppm) and to sweep a potential about a specified point with a scan of selected relative width. Thus, $E_2$ was accurately programmed to pass ions within a window of kinetic energies relative to the kinetic energy of the precursor ions.

Scanning the electric field of $E_2$ about that to transmit the 8-keV precursor ions produced a kinetic energy profile of the precursor ion. Scans over this profile were digitized and summed by a Nicolet 1170 signal averager, which employed a 12-bit analog-to-digital converter, and were stored as a channel of 1024 points. Subsequently, the electric field of the second ESA was changed by dividing the potentials on the electrodes of the second ESA by 2, to six significant figures, and the kinetic energy profile of the doubly charged molecular ion was recorded similarly in a second channel of the signal averager.

To measure the translational energy lost upon charge stripping of the precursor ion, the peak profile of the doubly charged ion was compared with the peak profile of the precursor ion. In the absence of translational energy loss in the charge-stripping process, the precursor and the doubly charged ion would appear at the same relative location in the scan. In fact, the doubly charged ion appears at a lower kinetic energy because there is an energy debit occurring in the electron removal process. The energy difference between the high-energy sides of the peak profiles was used to obtain an onset or $Q_{min}$ value[37,38] for the second ionization energy. This difference was extracted from the data by extrapolating the high-energy side of each peak to baseline, where the difference was measured. This extrapolation was usually performed on unsmoothed data. If the signal-to-noise ratio was low, the data were smoothed by using a second-order Savitzky–Golay algorithm to preserve underlying peak shape.

Oxygen was used as the collision gas in measurements of the apparent second ionization energies by charge stripping. The pressure in the collision cell was increased until the precursor ion beam intensity was reduced by 20%. The MS50-TA was also used to study the efficacy of various collision gases to produce charge stripping of $C_{60}^{\bullet+}$.

This ratiometric methodology was also used to measure the translational energy loss of product ions formed in high-energy collisions. Kinetic energy profiles were obtained as described for charge stripping except the electric field of $E_2$ was lowered by the factor of the ratio of the product/precursor ion masses. This ratio was multiplied by the

(35) We distinguish product ions as all ions that are products of the collision of precursor ions with the target gas, including collisionally excited but undissociated molecular ions, all ions that contain the target gas, and fragment ions. Fragment ions are those ions produced from a well-defined precursor species as a result of the loss of neutral fragments.

(36) Gross, M. L.; Chess, E. K.; Lyon, P. A.; Crow, F. W.; Evans, S.; Tudge, H. *Int. J. Mass Spectrom. Ion Phys.* **1982**, *42*, 243.

(37) Ast, T.; Porter, C. J.; Proctor, C. J.; Beynon, J. H. *Bull. Soc. Chim., Beograd* **1981**, *46*, 135.

(38) Cooks, R. G.; Beynon, J. H.; Ast, T. *J. Am. Chem. Soc.* **1972**, *94*, 1004. Porter, C. J.; Proctor, C. J.; Ast, H.; Beynon, J. H. *Int. J. Mass Spectrom. Ion Phys.* **1982**, *41*, 265. Kemp, D. L.; Cooks, R. G. In *Collision Spectroscopy*; Cooks, R. G., Ed.; Plenum Press: New York, 1978; Chapter 5. Stahl, D.; Maquin, F. *Chem. Phys. Lett.* **1984**, *108*, 613. Stahl, D.; Maquin, F.; Gaumann, T.; Schwarz, H.; Carrupt, P. A.; Vogel, P. *J. Am. Chem. Soc.* **1985**, *107*, 5049. Koch, W.; Schwarz, H.; Maquin, F.; Stahl, D. *Int. J. Mass Spectrom. Ion Processes* **1985**, *67*, 171. For a discussion of the error involved in the energy scale calibration, see: Langford, M. L.; Mathur, D.; Harris, F. M. *Rapid Commun. Mass Spectrom.* **1988**, *2*, 167. For a review, see: Ast, T. *Adv. Mass Spectrom.* **1986**, *10A*, 471.

precursor ion kinetic energy to give the value of $T_{exp}$, the expected kinetic energy of the product ion in the absence of translational energy loss. ($T_{exp}$ is equal to $T_4$ in eq 11). The parts per million difference in the relative position of the centroids obtained for the precursor ion and the product ion was measured. The translational energy loss, $\Delta T$, is this relative difference times the precursor ion kinetic energy and is denoted by $\Delta T = T_{exp} - T_{obs}$, where $T_{obs}$ is the experimentally observed kinetic energy of the product ion. Comparison of the derived and experimental kinetic energies of product ions formed from capture of the target gas was made by lowering the electric field of the second ESA by the factor of the ratio of the derived product ion kinetic energy over the precursor ion kinetic energy. In these latter experiments, the best agreement between the experimental kinetic energy and the derived one was obtained by closing the z-restrictor apertures located after the source and collector slits, and after the $\beta$ slits of the second ESA.

There is a fundamental advantage in using a three-sector ($E_1BE_2$) instrument instead of a reversed-geometry Nier–Johnson instrument (BE) for translational energy loss studies. For a reversed-geometry BE instrument, MS1 is comprised of a magnet only. Any drift in the magnetic field results in a change in the position of a peak in the kinetic energy scan because the precursor ion is focused in angle only. Lock devices and procedures were devised to compensate for this problem.[37,39] In the experiments reported here, MS1 was of forward-geometry Nier–Johnson design ($E_1B$) with the advantage of double focusing whereby precursor ions are focused in both angle and energy. In this case, the energy of the precursor ion was defined by the potential applied to the first ESA to which the accelerating potential is tightly coupled, both of which are more stable and more easily controlled than a magnetic field. Any drift in magnetic field moved the beam off of the collector slits located before the collision cell, and caused only a decrease in the height of the peak observed in the energy scan of $E_2$, not a shift in the location of the peak in the scan. Of course, an additional advantage of a double-focusing MS1 is that the precursor ion can be selected with higher resolution.

A benefit of ratioing the electric field of an ESA on a three-sector ($E_1BE_2$) instrument is that the accelerating potential need not be known accurately, only better than the largest experimental error. The accelerating potential was determined to better than 1%. The ratio of the electric fields of $E_2$ and $E_1$ and the $E_2$ electric field sweep width, however, do need to be accurately known and controlled by the MID.

**c. Four-Sector Tandem Mass Spectrometry.** A VG Analytical ZAB-T, a four-sector mass spectrometer, was also used for MS/MS experiments.[40] The first mass analysis stage, MS1, was a standard ZAB-SE of BE geometry. Ions were formed by EI with 70-eV electrons in a VG EI/CI source operated in the EI mode and heated to 300–350 °C. Precursor ions were accelerated to 8 keV, selected with a resolving power of approximately 1000, and subsequently subjected to high-energy collisions with target gases in the collision cell located after $E_1$ and before $B_2$, in the third field-free region. A constant $B_2/E_2$ linked scan, performed in conjunction with a Hall probe, was used to obtain the CAD spectra. A potential was applied to the collision cell for some experiments to decelerate the ion beam and reduce the center-of-mass collision energy. The linked scan was modified accordingly by the computer-controlled interface.

The second electrostatic analyzer was a segmented ESA of unique design and wide energy band-pass. One important feature of the second ESA is that, as MS2 is scanned in linked fashion, product ions whose kinetic energies were substantially shifted—from loss of translational energy during charge stripping or collisional activation[41] and/or from capture of the target gas—were accepted and transmitted to the detector under double-focused conditions. In addition, product ions at kinetic energies substantially different than the expected kinetic energy were accepted without being lost at $\beta$ slits (there are no $\beta$ slits after $E_2$).

Another advantage of the wide energy band-pass of the second ESA is that its voltage can be adjusted to bring the product ions to an optimum energy focus while still transmitting the precursor ion without slit discrimination. Typically, the voltage was lowered because the product ions were shifted to lower kinetic energy.[41] During the MS2 linked scan, the magnetic field was scanned downward from a value greater than that which transmitted the precursor ion beam. Data acquisition started when the ratio of $B_2/E_2$ (for the case of grounded collision cell) was equal to the precursor ion field value divided by the voltage of the second ESA before it was adjusted. Therefore, the scans in Figures 2, 5, 6, and 8–10 extend to $m/z$ values greater than that of the precursor ion. Experiments performed without decreasing the ESA voltage produced the same relative abundances of product ions, but ions at $m/z$ values greater than that of the precursor ion were not recorded. The experimental product ion masses obtained from the perturbed linked scan were lower than their true masses; however, the mass scale was corrected by changing the gain factor for the Hall probe calibration.

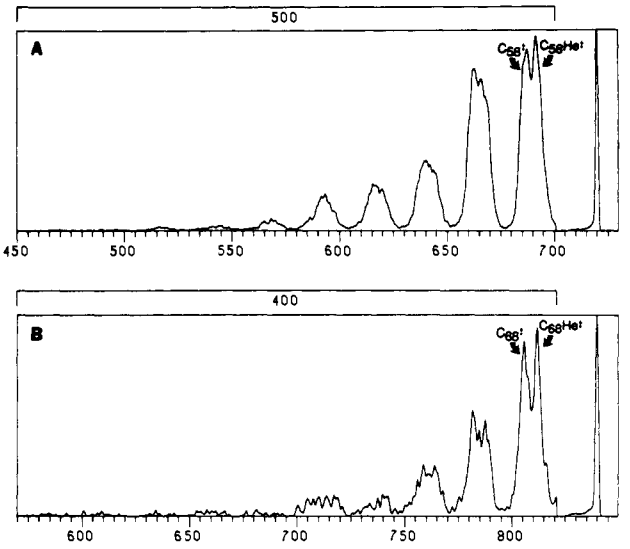


Figure 1. (A) Partial spectrum of product ions resulting from high-energy collisions of $C_{60}^{+}$ with He. (B) Partial spectrum of product ions resulting from high-energy collisions of $C_{70}^{+}$ with He. These spectra were obtained separately on the three-sector tandem mass spectrometer after reducing the precursor ion beams by 15%. The scan is from high to low energy (right to left), and the energy scale was converted to a mass scale by using the relationship given by eq 11. For a discussion of the assignment of the components of the doublet present at the $C_2$ loss regions, see section 1.e of the Results and Discussion.

## Results and Discussion

We studied the products of high-energy collisions of $C_{60}^{+}$ and $C_{70}^{+}$ with noble gases as well as with $D_2$, $N_2$, NO, and $O_2$ by using tandem mass spectrometry. The results are discussed according to the collision gas used. The amount of gas admitted to the collision cell was monitored by the degree that the precursor ion beam was suppressed, which is given in the figure captions or the text. In the absence of collision gas, one observes predominantly $C_2$ loss from both $C_{60}^{+}$[42-44] and $C_{70}^{+}$[44] by a so-called metastable ion decomposition.

**1. Helium Collision Gas. a. Product Ion Spectra.** The monatomic noble gases are the simplest collision gases. The spectra of products formed by high-energy CAD of $C_{60}^{+}$ and $C_{70}^{+}$ obtained with the three-sector instrument (see Figure 1) show that the predominant fragmentation pathways of $C_{60}^{+}$ and $C_{70}^{+}$ are the formal losses of sequential $C_2$ units. These may occur by consecutive $C_2$ loss or by the concerted loss of $C_2$, $C_4$, $C_6$, etc. Both possibilities were discussed in the literature for metastable ion decompositions,[42,43] collisional activation,[32-34a] and photodissociation.[45]

The MS/MS analysis of $C_{60}^{+}$ and $C_{70}^{+}$ was reported previously.[29,32-34] There are some differences in the spectra in Figure

(39) Morgan, R. P.; Beynon, J. H.; Bateman, R. H.; Green, B. N. *Int. J. Mass Spectrom. Ion Phys.* **1978**, *28*, 171.

(40) This instrument was commissioned by the Midwest Center for Mass Spectrometry, a former NSF regional instrumentation facility (Grant No. CHE 8620177). It was designed by Robert Bateman and built by VG Analytical (now Fisons Instruments) for the MCMS. The spectrometer known as a ZAB-T was briefly described by Gross, M. L. In *Methods in Enzymology, Mass Spectrometry*; McCloskey, J. A., Ed.; Academic Press: New York, 1990; Vol. 193, pp 131–153.

(41) (a) Neumann, G. M.; Sheil, M. M.; Derrick, P. J. *Z. Naturforsch.* **1984**, *39a*, 584. (b) Neumann, G. M.; Derrick, P. J. *Org. Mass Spectrom.* **1984**, *19*, 165. (c) Gilbert, R. G.; Sheil, M. M.; Derrick, P. J. *Org. Mass Spectrom.* **1985**, *20*, 431. (d) Sheil, M. M.; Derrick, P. J. *Org. Mass Spectrom.* **1988**, *23*, 429.

(42) Radi, P. P.; Hsu, M. T.; Brodbelt-Lustig, J.; Rincon, M.; Bowers, M. T. *J. Chem. Phys.* **1990**, *92*, 4817.

(43) Radi, P. P.; Hsu, M. T.; Rincon, M. E.; Kemper, P. R.; Bowers, M. T. *Chem. Phys. Lett.* **1990**, *174*, 223.

(44) Experiments performed at the University of Nebraska.

(45) O'Brien, S. C.; Heath, J. R.; Curl, R. F.; Smalley, R. E. *J. Chem. Phys.* **1988**, *88*, 220.

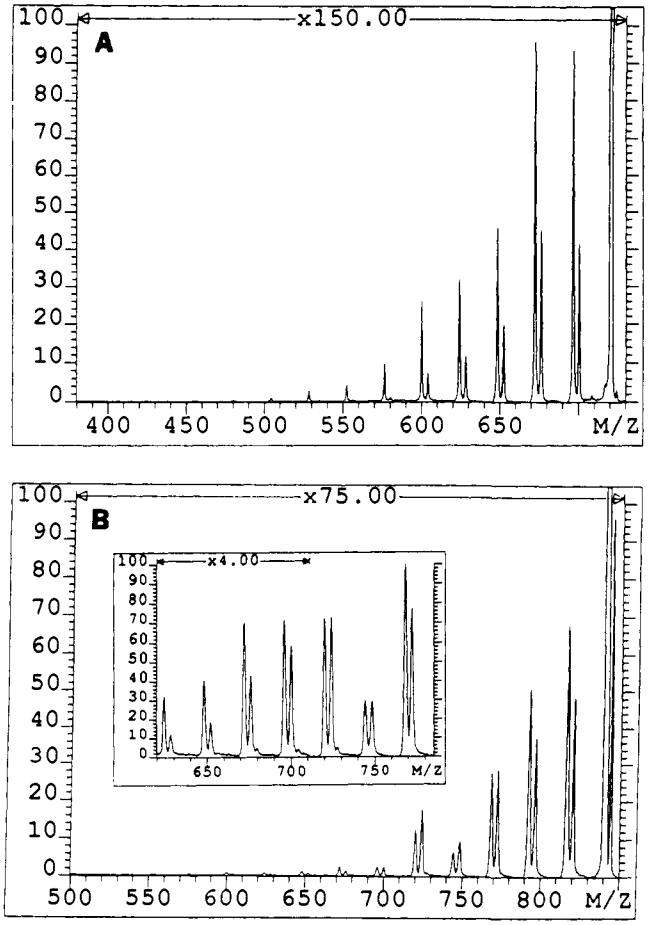


**Figure 2.** (A) Partial mass spectrum of product ions resulting from high-energy collisions of $C_{60}^{\bullet+}$ with He (40% beam suppression). (B) Partial mass spectrum of product ions resulting from high-energy collisions of $C_{70}^{\bullet+}$ with He (50% beam suppression). The data in the inset were obtained after 80% beam suppression. In each spectrum the fullerene precursor ion is offscale. The small peak to the left of the peak from the $C_{60}^{\bullet+}$ precursor ion is an artifact peak.

1 and those reported by Harrison and co-workers.[32] The precursor ions selected by MS1 for Figure 1A,B were $^{12}C_{60}^{\bullet+}$ and $^{12}C_{70}^{\bullet+}$, respectively, whereas the major $^{13}C$-containing species were not separated in the previous study in order to achieve higher sensitivity. This may explain why curious, partially resolved *doublets*[46] for the $C_2$ loss and other product ion peaks were not observed previously.[32] Each component of the doublet is shifted to a lower kinetic energy than that expected for a product ion produced by collisional activation in which the target gas is not incorporated in its precursor. Neither can be attributed to a contribution from the metastable loss because, in the absence of collision gas, the metastable $C_2$ loss peak appears at lower abundance and is not energy shifted, as is expected for a metastable ion decomposition.

A mass scale provided for Figure 1 shows that substantial shifts occur to lower masses, actually to lower kinetic energies, for the product ions (see section 2.a of the Experimental Section). The energy shifts tend to increase as the number of equivalent $C_2$ units lost increases, not only for He but for all of the collision gases investigated here. The magnitude of the energy shifts is greatest with the light collision gases.[47]

The $C_2$ loss doublet observed in Figure 1 motivated the use of a four-sector mass spectrometer. Such instruments provide higher resolution spectra for the second stage of mass analysis because the product ions are both energy and angle focused. Not only are the all-carbon product ions well-resolved, but also there are peaks 4 u higher, indicating that the He collision gas is incorporated *into* the product ions (Figure 2) as was previously shown by Schwarz and co-workers.[34a] Incorporation of the target gas into a product ion is unprecedented during high-energy collisional activation of other molecular ions. The doublet present in the $C_2$ loss peaks (Figure 1) is now clearly established to be a mass doublet.

Collision gas was added to give an ion beam attenuation of 40% for the spectrum in Figure 2A. At this degree of attenuation, single collisions predominate, and only relatively low abundance product ions are observed below $m/z$ 500. There is a notable drop in the equivalent $C_2$ loss fragmentation chemistry occurring after the $C_{50}$ product ions. This special behavior of $C_{50}$ was also observed in the long time scale metastable decay of photon-activated $C_{60}^{\bullet+}$.[45] Increasing the beam attenuation to 80–90%, the double and higher collision regime, enhances the relative abundance of all product ions, but especially those of low mass. A second envelope of ions dominated by odd-carbon species begins to appear below $C_{32}^{\bullet+}$, and the distribution of these product ions will be addressed in the discussion of $C_{60}^{\bullet+}$ collisions with neon target gas.

The spectrum in Figure 2B was obtained by attenuating the $C_{70}^{\bullet+}$ precursor ion beam by 50%. There is a smooth decline in the relative abundance of the product ions down to those of $C_{62}$. The increased relative abundance of the $C_{60}$ product ions precedes a sharp reduction in the product ion abundances for ions of $m/z$ below 720 and 724. The $C_{60}$ product ions are a kinetic and/or thermodynamic bottleneck in the fragmentation chemistry, similar to $C_{50}^{\bullet+}$ in the photofragmentation of $C_{60}^{\bullet+}$.[45] In addition, the He-containing $C_{60}He^{\bullet+}$ product ion is of greater abundance than the $C_{60}^{\bullet+}$ product ion, and this remains so up to about 80% beam attenuation, at which point the abundances of the two ions are approximately equal (see inset of Figure 2B). Product ions of $m/z$ less than 600 ($C_{50}^{\bullet+}$) are essentially absent at 40% beam attenuation and are of relatively low abundance at higher degrees of collisional activation.

**b. Direct Production of Fullerene Endohedral Complexes: $C_{60}He^{\bullet+}$, $C_{70}He^{\bullet+}$, $C_{84}He^{\bullet+}$, and $C_{60}He_2^{\bullet+}$.** The spectra taken with the four-sector mass spectrometer (Figure 2) show $C_{60}He^{\bullet+}$ and $C_{70}He^{\bullet+}$ ions at 4 u higher mass than that of the $C_{60}^{\bullet+}$ and $C_{70}^{\bullet+}$ precursor ions, respectively. This is a significant finding and represents direct production of noble gas $C_{60}^{\bullet+}$ and $C_{70}^{\bullet+}$ complexes. It is likely that the He atom is trapped within the fullerene cage, giving rise to endohedral complexes because the weak attractive forces between He and an organic ion would not allow a He atom to remain bound to the exterior of the fullerene ion during the time of flight from the collision cell to the detector. Helium capture by other organic ions is unprecedented in the rather long history of MS/MS. In addition to $C_{60}He^{\bullet+}$ and $C_{70}He^{\bullet+}$, we observed $C_{84}He^{\bullet+}$ in the MS/MS analysis of the products of $C_{84}^{\bullet+}$ collisions with He. Although the *direct* production of these species was not reported by Schwarz and coworkers[34a] in their pioneering study, the observation of $C_{60}He^{\bullet+}$ was independently made by Ross and Callahan.[34b]

For 8-keV collisions of $C_{70}^{\bullet+}$ with He, $C_{70}He^{\bullet+}$ is the most abundant product ion up to about 80% beam reduction, at which point $C_{68}^{\bullet+}$ becomes the dominant product ion and $C_{70}He^{\bullet+}$ the second most abundant. This indicates an extreme ruggedness for the $C_{70}He^{\bullet+}$ ion, which is surviving multiple collisions under these latter conditions.

Under multiple-collision conditions, capture of two helium atoms can be effected. For example, both He-containing product ions and a short series of ions corresponding to the capture of two He atoms starting at about $C_{52}He_2^{\bullet+}$ and continuing to approximately $C_{64}He_2^{\bullet+}$ (see inset of Figure 2B and ref 1) were observed for 8-keV collisions of $C_{70}^{\bullet+}$ with He (>40% beam suppression).[48] Apparently a second He atom can be captured by the first-generation He-containing product ions. The absence of higher carbon number ions containing two heliums may be the result of "cooling"

(46) The resolution is not sufficient to allow the elimination of the possibility of more closely spaced multiplets.

(47) Gross, M. L.; Tomer, K. B.; Cerny, R. L.; Giblin, D. E. In *Mass Spectrometry in the Analysis of Large Molecules*; McNeal, C. J., Ed.; John Wiley and Sons: New York, 1986; p 171.

(48) It is difficult to discern the exact bounds of this ion series owing to the low abundance of these ions.

**Scheme I**

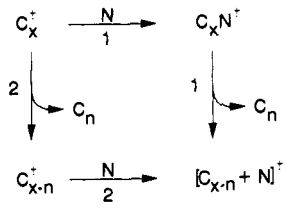

of the endohedral complex containing two heliums by loss of consecutive $C_2$ units (or intact $C_n$ units).

The possibility of the trapping of atoms, especially metals, inside of intact all-carbon cages was investigated by Smalley and co-workers[49,50] and others.[51] The entrapment of the metal was assumed to occur during the closure of the fullerene produced by laser vaporization of a graphite disk that had been impregnated with a metal salt. This entrapment scheme is analogous to the formation of a carcaplex from the closure of two cavitands in the host–guest chemistry elaborated by Cram[52] and Cram et al.,[53] and contrasts dramatically with the method used here to insert the guest atom.

We build on previous arguments that the fullerene carbon cages can entrap He[34] and metal ions.[49,50] If one draws on a host–guest chemistry analogy to name the species involved in the production of the He-containing product ions, then the fullerene ions are spherands in the gas-phase high-energy reaction that produces the He-entrapped spheraplex. Spherands are defined as "...hosts conformationally organized prior to complexation",[54a] and "the spherands contain cavities in their uncomplexed state which become filled upon complexation. Thus, the spherands are rigidly organized for complexation during their synthesis rather than during their complexation".[54b] From host–guest chemistry terminology, the He-captured product ions are classified as capsular complexes. "The term capsular complex is reserved for those structures in which the guest surface is covered well enough by the host to prevent ligand or solvent from contacting the guest".[54a] The name endohedral ("in the cage") complex for a $C_{60}$ molecule with atoms or ions trapped inside was suggested more recently.[51]

**c. Mechanism of Helium Incorporation.** Because the carbon network is already formed, the incorporation of He into the fullerene molecular ions must proceed by a different mechanism than that of metal incorporation and that producing carcaplexes. That is, the formation of $C_{60}He^{\bullet+}$ and $C_{70}He^{\bullet+}$ indicates that either the carbon cage was unruptured during the entrapment event and the He passed through a hexagonal or pentagonal ring or the cage was ruptured and reclosed before the He could escape. In either case, the entrapment of He by $C_{60}^{\bullet+}$ and $C_{70}^{\bullet+}$ starts with an intact carbon cage. The He is not loosely bound to the exterior of the fullerene ions, as was also argued by Schwarz and co-workers.[34a]

There are two mechanisms leading to product ions containing the target gas, and they are listed in Scheme I as the clockwise and counterclockwise mechanisms 1 and 2, respectively, where $x$ = 60, 70, or 84, $n$ is an integer, usually even, and N is the collision gas. Whether the $C_n$ neutral lost is an intact $C_n$ unit or the elements of $C_n$ has not been clearly established.

(i) **Mechanism 2.** One possible mechanism is collision-induced fracture of the carbon cage of $C_{60}^{\bullet+}$ followed by capture of He by the fragment ions. The abundance of the He-containing product ions produced from mechanism 2 should increase more rapidly with target gas pressure than those produced from mechanism 1 because two collisions are required to produce the product ion by mechanism 2. Unfortunately, it is difficult to know the pressure inside of the collision cell. The most accessible experimental parameter related to the total number of product ion collisions is the percentage by which the precursor ion beam is attenuated after the addition of collision gas.[56] By measuring the peak heights of both the He-containing as well as the all-carbon product ions produced from the high-energy collisions of $C_{60}^{\bullet+}$ with He collision gas at increasing beam attenuations, we obtain the graphs in Figure 3. The region from 10% to 40% beam reduction is linear, indicating predominantly single-collision conditions. The shape in the graphs after approximately 50% beam reduction is parabolic, indicating a multiple-collision regime. The ratio of the He-containing product ions, $[C_{60-n} + He]^{\bullet+}$, to the $[C_{60-n}]^{\bullet+}$ product ions increases slowly as the percent beam reduction increases. The ratio at 90% beam reduction is 30–50% greater than the value at 10% beam reduction. This is more likely the result of increased collision-induced He losses from those He-containing product ions undergoing second collisions rather than increased production of He-containing product ions by mechanism 2.

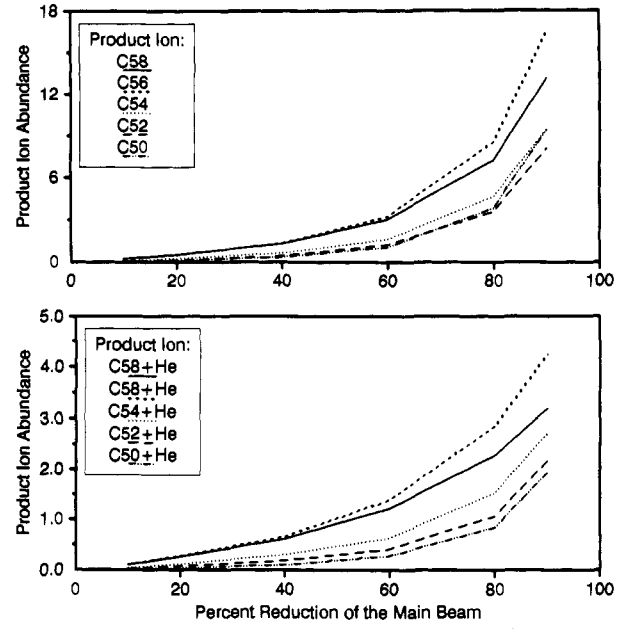


**Figure 3.** Absolute abundances (arbitrary units) of the all-carbon and the He-containing product ion peaks for increasing attenuation of a $C_{60}^{\bullet+}$ ion beam by He.

**Scheme II**

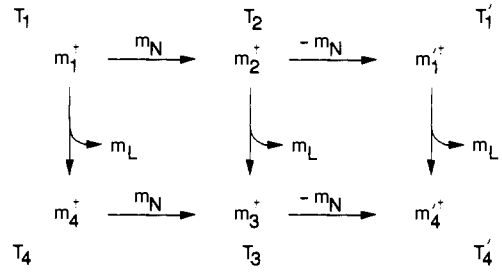

(ii) **Mechanism 1.** In mechanism 1, the He-containing product ions are produced from the incorporation of the target gas into the all-carbon cage with subsequent (or concomitant) loss of neutral $C_n$ fragments. Required for mechanism 1 is the production of $C_{60}He^{\bullet+}$ and $C_{70}He^{\bullet+}$ prior to loss of $C_n$ neutrals, as is observed. It is also expected, on the basis of this mechanism, that the higher carbon number He-containing product ions should fragment to produce lower carbon number He-containing product ions. Indeed,

(49) Heath, J. R.; O'Brien, S. C.; Zhang, Q.; Liu, Y.; Curl, R. F.; Kroto, H. W.; Tittel, F. K.; Smalley, R. E. *J. Am. Chem. Soc.* **1985**, *107*, 7779.
(50) Weiss, F. D.; Elkind, J. L.; O'Brien, S. C.; Curl, R. F.; Smalley, R. E. *J. Am. Chem. Soc.* **1988**, *110*, 4464.
(51) Cioslowski, J.; Fleischmann, E. D. *J. Chem. Phys.* **1991**, *94*, 3730.
(52) Cram, D. J. *Science* **1988**, *240*, 760.
(53) Cram, D. J.; Karbach, S.; Kim, Y. H.; Baczynskyj, L.; Marti, K.; Sampson, R. M.; Kalleymeyn, G. W. *J. Am. Chem. Soc.* **1988**, *110*, 2554.
(54) (a) Cram, D. J.; Trueblood, K. N. *Top. Curr. Chem.* **1981**, *98*, 43. The subject of this entire volume is host–guest chemistry. (b) Cram, D. J. *Science* **1983**, *219*, 1177.
(55) (a) Heymann, D. *J. Geophys. Res.* **1986**, *B91* (B13), E135–E138. (b) Lewis, R. S.; Srinivasan, B.; Anders, E. *Science* **1975**, *190*, 1251. (c) Niemeyer, S.; Marti, K. *Proc. Lunar Planet. Sci.* **1981**, *12B*, 1177.
(56) Holmes, J. L. *Org. Mass Spectrom.* **1985**, *20*, 169.

Schwarz and co-workers[34a] reported that mass-selected $[C_{x-n}He]^{\bullet+}$ ions undergo unimolecular loss of $C_2$ rather than a helium atom. Furthermore, Ross and Callahan[34b] showed that collisional activation of $C_{60}He^{\bullet+}$ (with Xe collision gas) leads to both $C_xHe^{\bullet+}$ and $C_x^{\bullet+}$ product ions by loss of $C_n$ units in parallel with He loss, demonstrating that $C_x^{\bullet+}$ product ions are produced in part from the $C_{60}He^{\bullet+}$ fullerene endohedral complex. It is not clear, however, whether *all* of the $C_x^{\bullet+}$ product ions arise from the $C_{60}He^{\bullet+}$ or $C_{70}He^{\bullet+}$ endohedral complexes.

**d. Energetic Considerations of Target Gas Capture.** We now present a derivation of the kinetic energies expected for product ions formed from the capture of the target gas and compare them with the experimental values. As an aid, we present Scheme I as the left half of Scheme II, with the ions represented by their masses, where $T_{1-4}$ are the kinetic energies of the respective ions with masses $m_{1-4}$, and $m_N$ is the mass of the target gas. The mass of the neutral fragments lost is designated $m_L$. The right half of Scheme II contains the possibility of producing $[M - C_n]^{\bullet+}$ product ions by incorporation of the target gas into the molecular ion, followed by loss of $C_n$, and then loss of the target gas (or vice versa). For this process, the mass of the final product ion is the same as a product ion that did not capture and lose a target gas; however, the kinetic energy is changed, as indicated by the prime.

The relationships between the masses are

$$m_2 = m_1 + m_N \tag{1}$$

$$m_3 = m_2 - m_L = m_1 + m_N - m_L \tag{2}$$

$$m_4 = m_1 - m_L \tag{3}$$

$$m_3 = m_4 + m_N \tag{4}$$

The initial kinetic energy of the precursor ion, $m_1^{\bullet+}$, is $T_1$. All product ion kinetic energies will be related to this kinetic energy.

The kinetic energy of the fullerene endohedral complex formed by capturing the target gas, N, is $T_2$. This corresponds to the process $m_1^{\bullet+} \rightarrow m_2^{\bullet+}$ in Scheme II. Because the momentum must be the same before and after the collision, we equate the momentum of the projectile ion before and after the capture of N

$$m_1\bar{v}_1 = (m_1 + m_N)\bar{v}_2 \tag{5}$$

Taking dot products of each side of eq 5 produces scalar quantities

$$m_1^2v_1^2 = (m_1 + m_N)^2v^2 \tag{6}$$

and substituting for the kinetic energies of $m_1$ and $m_2$, we find the relationship between $T_1$ and $T_2$:

$$2m_1T_1 = 2(m_1 + m_N)T_2 \tag{7}$$

$$T_2 = \frac{m_1}{m_2}T_1 = \left(\frac{m_1}{m_1 + m_N}\right)T_1 \tag{8}$$

The magnitude of $T_3$, the kinetic energy of the $[C_{x-n} + N]^{\bullet+}$ product ions which are represented by $m_3^{\bullet+}$, depends on whether $m_3^{\bullet+}$ is produced by the clockwise or the counterclockwise mechanism. We now derive $T_3$ from each mechanism, by considering conservation of energy, and explore other aspects of the energetics associated with target gas capture.

The kinetic energy of $m_3^{\bullet+}$ produced from the clockwise mechanism is

$$T_{3,CW} = (m_3/m_2)T_2 \tag{9}$$

Substituting eq 8 for $T_2$ and eqs 1 and 2 for $m_2$ and $m_3$, respectively, we obtain

$$T_{3,CW} = \frac{m_1(m_1 + m_N - m_L)}{(m_1 + m_N)^2}T_1 \tag{10}$$

which is the kinetic energy of the $[C_{x-n} + N]^{\bullet+}$ product ions formed from mechanism 1, Scheme I.

Consider now the counterclockwise path for arriving at $m_3^{\bullet+}$:

$$T_4 = (m_4/m_1)T_1 \tag{11}$$

and

$$T_{3,CCW} = (m_4/m_3)T_4 \tag{12}$$

Substituting eq 11 for $T_4$ and eqs 2 and 3 for $m_3$ and $m_4$, respectively, we obtain

$$T_{3,CCW} = \frac{(m_1 - m_L)^2}{m_1(m_1 + m_N - m_L)}T_1 \tag{13}$$

Both expressions (eqs 10 and 13) give the kinetic energies of the products in terms of the masses of the precursor ion, the neutral lost, and the target gas.

The kinetic energy expected for a fragment ion produced from conventional collisional activation is $T_4$.[57] This is given by eq 11.

The kinetic energy of a product ion, $m_1'^{\bullet+}$, formed first from capture of the target gas, N, and then by its expulsion is

$$T_1' = \left(\frac{m_1}{m_1 + m_N}\right)T_2 = \left(\frac{m_1}{m_1 + m_N}\right)^2T_1 \tag{14}$$

Although the mass of the empty fullerene ion $m_1'^{\bullet+}$ is ultimately unchanged (Scheme II), its kinetic energy is decremented twice because N is incorporated and then lost.

A product ion that has captured the target gas, N, lost the target gas, and then lost a neutral species, L, is represented by $m_4'^{\bullet+}$ and has a kinetic energy of

$$T_4' = \left(\frac{m_1 - m_L}{m_1}\right)T_1' = \frac{m_1(m_1 - m_L)}{(m_1 + m_N)^2}T_1 \tag{15}$$

The value of $T_4'$ is the same if the order of the losses is reversed, and it would be slightly lower if $m_4'^{\bullet+}$ were produced from an $m_3^{\bullet+}$ intermediate formed by mechanism 2, Scheme I.

**e. $C_{60}He^{\bullet+}$ and $C_{70}He^{\bullet+}$ as the Major Precursor of the Product Ions from He Collisions.** Comparison of the predicted and experimental kinetic energies of the product ions allows the components of the doublets in the spectra in Figure 1 to be assigned and also provides insight into the mechanism of the formation of the product ions. We studied the kinetic energies of product ions produced from 8-keV collisions of both $C_{60}^{\bullet+}$ and $C_{70}^{\bullet+}$ with He (and other) target gases by using the three-sector mass spectrometer, which is well-suited for measurement of product ion kinetic energies. We focus on the $C_{70}$ system to illustrate the results. The widths of the product ion peaks corresponding to ions formed by loss of $C_n$ from, for example, $C_{70}N^{\bullet+}$, are narrower than those produced by loss of $C_n$ from $C_{60}N^{\bullet+}$ because the kinetic energy releases associated with the loss of the $C_n$ are less for $C_{70}N^{\bullet+}$. The practical result is that the peaks contributing to a doublet are more completely resolved for the $C_{70}$ system. This effect is demonstrated for the $C_2$ loss doublets in Figure 1.

In the process $C_{70}^{\bullet+} \rightarrow C_{70}He^{\bullet+} \rightarrow C_{68}He^{\bullet+}$, all of the center-of-mass collision energy is imparted into the intermediate $C_{70}He^{\bullet+}$ product ion. Fragmentation of this intermediate will be analogous to a metastable loss from internally excited $C_{70}He^{\bullet+}$, and the kinetic energy of $C_{68}He^{\bullet+}$ is exactly $T_{3,CW}$. The experimental kinetic energy of $C_{68}He^{\bullet+}$ was compared directly to that predicted by $T_{3,CW}$ by acquiring the $C_{70}^{\bullet+}$ peak profile and, after reducing the potential on the second ESA by the factor given by eq 16, acquiring the peak profile of the product ion. In this

$$\frac{T_{3,CW}}{T_1} = \frac{m_1(m_1 + m_N - m_L)}{(m_1 + m_N)^2} \tag{16}$$

experiment, the $C_{68}He^{\bullet+}$ product ion profile should appear at the same location in the scan as that of the precursor ion, as is observed (see Figure 4). We assign $C_{68}He^{\bullet+}$ to the component of the doublet that lines up with the precursor ion peak. This result is

(57) For conventional collisional activation depicted by the process $m_1 \rightarrow m_4$, the actual kinetic energy of the fragment ions will be less owing to the conversion of kinetic energy to internal energy to drive the fragmentation thermochemistry. Any kinetic shift will further shift the observed kinetic energy of a fragment ion to lower energy, but not lower than the value of the center-of-mass collision energy. For a discussion of kinetic shift, see: Lifshitz, C. *Mass Spectrom. Rev.* **1982**, *1*, 309. See also the Experimental Section.

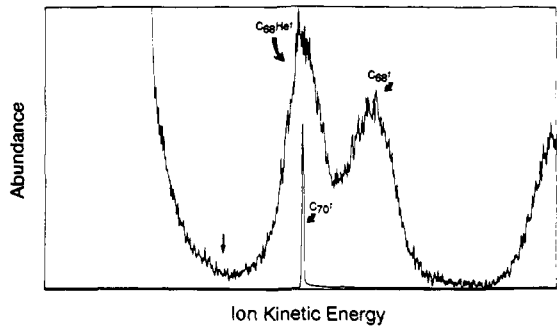


Figure 4. Kinetic energy profile of $C_{68}He^{\bullet+}$, top trace, overlayed with the profile of the $C_{70}^{\bullet+}$ precursor ion. The sweep width was 60 000 ppm, and the scan is from high to low kinetic energy (left to right). The arrow marks the region in the scan where $C_{68}^{\bullet+}$ product ions formed from collisional activation in which He is not captured would appear. The low-energy foot of $C_{70}^{\bullet+}$ is offscale in the beginning of the top trace. The data presented are the raw, unsmoothed data. See Sections 2.b of the Experimental Section and 1.e of the Results and Discussion for details.

also consistent with mechanism 1 in Scheme I as the route to the formation of the He-containing product ions. Similar results were obtained from the analysis of the kinetic energy of other He-containing product ions formed from both $C_{60}^{\bullet+}$ and $C_{70}^{\bullet+}$. The low-energy direction is reversed for the scan in Figure 4 from those in Figure 1; therefore, the composition of the component of the doublets closest to the main beam in Figure 1 is $C_{58}He^{\bullet+}$ and $C_{68}He^{\bullet+}$ for Figure 1A,B, respectively.

The other component of the doublet shown in Figure 4 is shifted to even lower kinetic energy. We attribute $C_{68}^{\bullet+}$ to this second component. This $C_{68}^{\bullet+}$ product ion can be formed from loss of He from $C_{68}He^{\bullet+}$ or from loss of He followed by loss of $C_2$ from $C_{70}He^{\bullet+}$. The latter process is easily distinguished from the process $C_{70}^{\bullet+} \rightarrow C_{68}^{\bullet+}$ (i.e., for conventional collisional activation). The $C_{68}^{\bullet+}$ fragment ions produced from this process would have a kinetic energy close to $T_4$ and would appear in the region marked with an arrow in Figure 4. The $C_{68}^{\bullet+}$ appears at a lower energy than $C_{68}He^{\bullet+}$ because some kinetic energy is partitioned to the He lost from $C_{68}He^{\bullet+}$ (or to the He lost from $C_{70}He^{\bullet+}$ preceding $C_2$ loss). On the basis of the analysis of the product ion kinetic energies, we conclude that the endohedral complexes $C_{60}He^{\bullet+}$ and $C_{70}He^{\bullet+}$ are the major precursor species giving rise to the product ions (Figures 1 and 2) that contain and do not contain He.

**f. Importance of $T_3$ in the Analysis of He-Captured Product Ions by MS2.** It is important to note that in neither process forming $m_3^{\bullet+}$ (Scheme II) is $T_3$ equal to the kinetic energy predicted by eq 17. This fact bears on the ability of MS2 to accept

$$T_{3,exp} = (m_3/m_1)T_1 \qquad (17)$$

product ions that contain the target gas. When MS2 is scanned in a constant $B_2/E_2$ linked scan fashion, as the electric field of the ESA is scanned past the value to transmit ions with a nominal kinetic energy of $T_{3,exp}$, the magnetic field will be at a value to transmit $m_3^{\bullet+}$; however, $m_3^{\bullet+}$ does not have kinetic energy $T_{3,exp}$ expected for a straightforward fragmentation of $m_1^{\bullet+}$. For transmission through MS2 to be successful, the energy band-pass of $E_2$ must be adequate to transmit $m_3^{\bullet+}$ ions with kinetic energies of $T_{3,CW}$ or $T_{3,CCW}$, depending on the mechanism by which $m_3^+$ is produced. Because both $T_{3,CW}$ and $T_{3,CCW}$ are functions of the mass of the target gas, this effect will be more pronounced for more massive target gases (vide infra). The four-sector instrument is designed to provide wide band-passes for both $B_2$ and $E_2$ (see Experimental Section).

**g. Internal Energy of the He-Captured Molecular Ions and the Prospects of Synthesizing $C_{60}He$.** The capture of a He atom by $C_{60}^{\bullet+}$ and $C_{70}^{\bullet+}$ occurs by a completely inelastic collision, resulting in a complete conversion of all available center-of-mass collision energy (eq 18, where $T_c$ is the precursor ion kinetic energy at the time of the collision) into internal energy of the product ion containing the target gas. The implication of target gas capture on the internal energy of the resultant product ion was considered

$$E_{cm} = \left(\frac{m_N}{m_N + m_1}\right)T_c \qquad (18)$$

previously by Derrick and co-workers.[41a] For 8-keV $C_{60}^{\bullet+}$ collisions with He, $E_{cm}$ = 44 eV and for $C_{70}^{\bullet+}$ with He, $E_{cm}$ = 38 eV. Internal energies of that magnitude seem difficult to accommodate. Bowers and co-workers[43] in a study of the metastable decompositions of nonthermalized $C_{60}^{\bullet+}$ produced from laser vaporization of graphite determined that precursor ions with 39 eV of internal energy were responsible for the production of $C_{58}^{\bullet+}$. To produce more extensive fragmentation on the time scale of mass spectrometry, one needs to add more than 39–44 eV of internal energy; the internal energy imparted to the precursor ion during the ionization event and remaining in the ion during the time of flight from the ion source to the collision cell is expected to be substantially less than the internal energy increase resulting from high-energy collisions and capture of the target gas.

Survival of detectable $C_{60}He^{\bullet+}$ and $C_{70}He^{\bullet+}$, formed with large internal energies, in high vacuum, is a testament of the stability of these fullerene endohedral complexes and suggests that it is possible to synthesize condensed-phase $C_{60}He$ and $C_{70}He$. Endohedral complexes of inert gases and $C_{60}$ have been postulated[55a] to be the carriers of noble gases, including He and Ne, that were released upon heating carbonaceous material obtained from meteorites.[55] In an experiment performed by Niemeyer and Marti,[55c] graphite was laser vaporized in the presence of Ne, Ar, Kr, and Xe. The isolated carbonaceous condensate contained all of these gases, which were detected during stepwise heating of the material to 1000 °C.[55c] Synthesis of condensed-phase $C_{60}He$ and $C_{70}He$ would allow the temperature release profiles of these well-defined materials to be compared with those from meteoritic debris to assess the importance of fullerene endohedral chemistry in interstellar space.

To increase the observed abundance of $C_{60}He^{\bullet+}$, the collision cell following MS1 of the four-sector instrument was floated to a potential higher than ground potential. This reduces the internal energy of $C_{60}He^{\bullet+}$ produced in the sticking collision because $T_c$ is diminished, reducing $E_{cm}$ (see eq 18). The spectra (Figure 5) show that $C_{60}He^{\bullet+}$ becomes the most abundant product ion when the collision cell is floated to 4 kV ($E_{cm}$ = 22 eV).

The increased abundance of $C_{60}He^{\bullet+}$ when $T_c$ = 4 keV and $E_{cm}$ = 22 eV is due to lower internal energy uptake by the $C_{60}He^{\bullet+}$. Lower internal energy also manifests itself by the reduced abundances of $C_{58}He^{\bullet+}$, $C_{56}He^{\bullet+}$, etc., which are expected if these ions are produced from the $C_{60}He^{\bullet+}$ species via mechanism 1 (see Scheme I). According to this mechanism, if the $C_{60}He^{\bullet+}$ is formed with lower internal energy, then this ion would fragment less by the loss of $C_n$. Loss of the He atom from $C_{60}He^{\bullet+}$, $C_{58}He^{\bullet+}$, $C_{56}He^{\bullet+}$, etc. could occur along with loss of $C_n$, and that would produce the $C_{58}^{\bullet+}$, $C_{56}^{\bullet+}$, $C_{54}^{\bullet+}$... ion series.

As might be expected, the extent to which $C_n$ loss occurs and the absolute abundance of the resulting product ions decrease as $E_{cm}$ is reduced. (Note the gain factors in Figure 5.) In particular, there is no longer a detectable $C_{59}^{\bullet+}$ fragment at $m/z$ 708, which is produced when $T_c$ = 8 keV (see also Figure 2A).

When the collision cell is floated to 6 kV ($E_{cm}$ = 11 eV), the extent of $C_n$ loss fragmentation is reduced even further. The abundance of $C_{60}He^{\bullet+}$, however, is also decreased, along with its He-containing fragment ions. The cross section for formation of $C_{60}He^{\bullet+}$ as a function of collision energy has a maximum in the kiloelectronvolt range. The maximum arises because, as the collision energy is increased, the cross section for inserting He increases whereas the lifetime of the adduct decreases.

The $C_{60}He^{\bullet+}$ product ion was also detected when the center-of-mass collision energy was 4.4 eV (collision cell floated to 7.2 kV). This establishes an upper limit of 4.4 eV for the activation energy for the insertion of He into the $C_{60}^{\bullet+}$ cage. Furthermore, this observation can be taken to overrule the hypothesis that the bonding is of $C_{60}^{\bullet+}$ to excited He or of neutral $C_{60}$ to $He^{\bullet+}$, given that promotion and ionization energies of He exceed 19 eV.

The deposition of the center-of-mass energy into internal energy of the He-captured molecular ion has implications for the detection

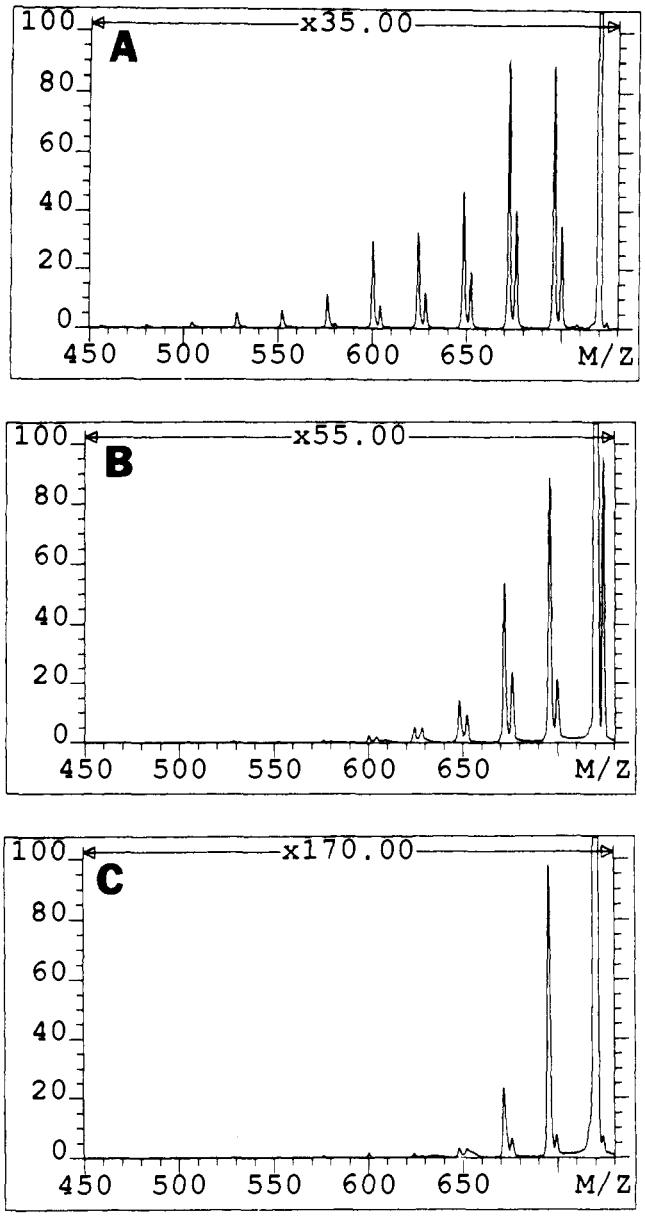


**Figure 5.** Partial mass spectra of product ions resulting from high-energy collisions of $C_{60}^{\bullet+}$ with He. The collision cell was floated to 0 kV (A), 4 kV (B), and 6 kV (C). The pressure of He target gas was the same for each experiment and produced a beam suppression of 60% when the collision cell was unfloated.

of other He-containing fullerene molecular ions. From eq 18, $E_{cm}$ is decreased as the mass of the fullerene molecular ion is increased; therefore, the internal energy of the He-containing product ion also is decreased. Indeed, for 8-keV precursors, the $C_{60}He^{\bullet+}$ is of lower relative abundance than $C_{70}He^{\bullet+}$, which is of lower abundance than $C_{84}He^{\bullet+}$ (see Figures 2 and 6). In fact, the $C_{84}He^{\bullet+}$ product ion is 3 times as abundant as $C_{82}^{\bullet+}$, the second most abundant product ion. Moreover, the capture of He appears to be a property of caged carbon ions and can be used as evidence to characterize unknown cage structures.

**h. Kinetic Energy of the He-Containing Molecular Ions.** The kinetic energy of $C_{60}N^{\bullet+}$ or $C_{70}N^{\bullet+}$, $T_2$, is simply the kinetic energy of the precursor ion, $T_1$, minus the center-of-mass collision energy. Because $T_2$ is proportional to $T_1$, the ratio of the kinetic energies of the product ion containing the target gas and the precursor ion is independent of $T_1$

$$\frac{T_2}{T_1} = \frac{m_1}{m_1 + m_N} \tag{19}$$

We obtained the kinetic energy profiles depicted in Figure 7 by reducing the electric field of the second ESA by the ratio given

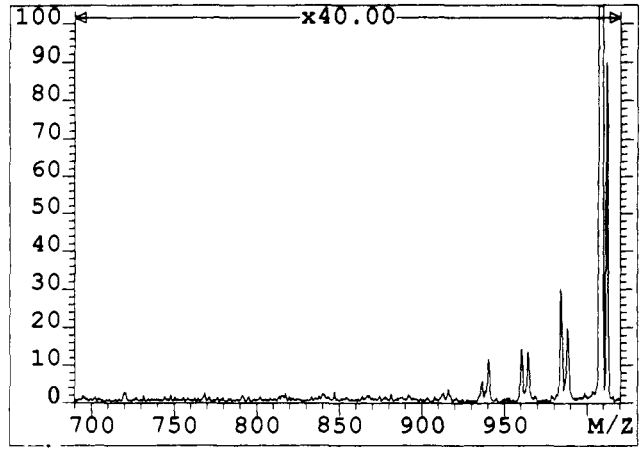


**Figure 6.** Partial mass spectrum of product ions resulting from high-energy collisions of $C_{84}^{\bullet+}$ with He (50% beam suppression). The peak from the $C_{84}He^{\bullet+}$ product ion appears to the right of that from the precursor ion.

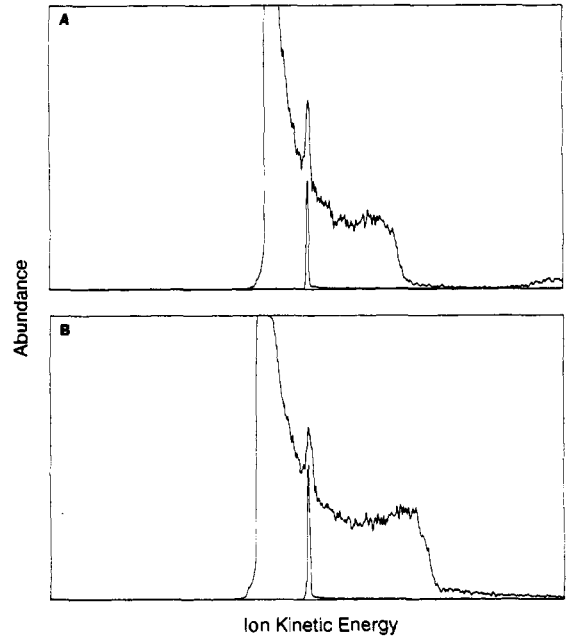


**Figure 7.** Kinetic energy profile of the low-energy foot (top trace), obtained after decreasing the potential on the second ESA by the factor given by eq 19, overlayed with the profile of the (A) $C_{60}^{\bullet+}$ and (B) $C_{70}^{\bullet+}$ precursor ions, lower trace. The sweep width was 60 000 ppm, and the scan is from high to low kinetic energy (left to right). The kinetic energy of the precursor ions was 4 and 8 keV for (A) and (B), respectively. The $C_{60}He^{\bullet+}$ and $C_{70}He^{\bullet+}$ product ions appear as the narrow peaks in the low-energy tail at the kinetic energy, $T_2$, predicted for a product ion formed from capture of a He atom (see section 1.h of the Results and Discussion).

by eq 19 for He target gas. The appearance of a sharp peak, located in the foot of the low-energy tail of the main beam, is attributed to $C_{60}He^{\bullet+}$ and $C_{70}He^{\bullet+}$. The extended low-energy foot in Figure 7, which is also apparent in Figure 1, is a characteristic peak shape of parent ions colliding with He[47] and provides some information on the collision dynamics. The foot is composed of ions that have undergone both elastic and inelastic collisions with the target gas. In an inelastic collision, some of the center-of-mass collision energy is converted into internal energy modes of the system. In this case, the foot is composed of ions that have converted insufficient collision energy into internal energy to induce decomposition during the time of flight from collision to detection.[47]

The maximum kinetic energy a projectile ion can lose occurs in an elastic "head-on" collision and is $4E_{cm}$.[58] This loss of the

kinetic energy of the projectile ion in the forward direction is manifested as recoil momentum of the target gas. A lesser component of the kinetic energy is lost in glancing collisions.

A semiquantitative measure of the magnitude to which the foot extends to low energy can be obtained by extrapolating the abrupt descent on the right side of the low-energy tail to baseline, and taking the difference of the kinetic energy at this point from the precursor ion kinetic energy. For 8-, 4-, and 2.9-keV $C_{60}^{\bullet+}$ collisions with He at 25% beam reduction, the tail extends to approximately 150, 83, and 62 eV lower energy than the center of the main beam peak. These values are 84%, 94%, and 98%, respectively, of the maximum value $4E_{cm}$. Direct collisions of $C_{60}^{\bullet+}$ with He must be occurring, which are expected if the helium is to be incorporated into the $C_{60}^{\bullet+}$ ion. For 8- and 4-keV $C_{70}^{\bullet+}$ collisions with He after 25% beam reduction, the analogous values are 86% and 95%. These values are not a consequence of multiple collisions, because for 8-keV $C_{60}^{\bullet+}$, the magnitude of the low-energy tail is the same at 15% beam reduction as for 25% and higher beam reductions. As the beam reduction is increased beyond approximately 50%, however, a second foot begins to appear at even lower kinetic energy than the one shown in Figure 7.

**i. End Point of $C_n$ Loss and the Internal Diameter of $C_{60}^{\bullet+}$.** For He collisional activation under predominantly single-collision conditions (20% beam reduction), fragmentation occurs to produce ions down to at least $C_{38}^{\bullet+}$, $m/z$ 456. This does not appear to be a fragmentation end point, only the limit for which we can confidently say ions are detected at an acceptable signal to noise ratio. Under multiple-collision conditions (90% mean beam attenuation), we observe equivalent $C_2$ loss fragmentation proceeding to $C_{32}^{\bullet+}$, below which both even and odd carbon number fragments are observed down to at least $C_9^{\bullet+}$.

Results from laser-induced fragmentation experiments indicate that $C_{32}^{\bullet+}$ is the end point for loss of the elements of consecutive $C_2$ units from $C_{60}^{\bullet+}$, and it was suggested that $C_{32}^{\bullet+}$ was the smallest all-carbon cage molecule produced in the beam experiments.[45] Below $C_{32}^{\bullet+}$, there is a break in the losses down to approximately $C_{25}^{\bullet+}$. Below $C_{25}^{\bullet+}$, even and odd carbon number photofragments are observed. These low mass even/odd carbon number fragments were most easily detected when relatively high laser fluences were used.[45]

The He-containing product ions in Figure 2A also have an end point for $C_2$ loss, analogous to the end point for detection of metal ion containing fullerenes produced in laser vaporization of metal-impregnated graphite disks.[49,50] In the latter experiments, $C_{44}K^+$, $C_{44}La^+$ (possibly $C_{42}La^+$), and $C_{48}Cs^+$ were the smallest fullerene ions containing a metal ion.[50] The ionic radii of the noble gas configuration ions $K^+$ and $Cs^+$ are 1.4 and 1.7 Å, respectively.[59] The lowest carbon number He-containing product ion unambiguously detected here is $C_{44}He^{\bullet+}$ at high percent beam reductions. The van der Waals radius of He is 1.4 Å,[59] and the end point is, perhaps fortuitously, the same as for the $K^+$-containing fullerenes.

The C-center to C-center internal diameter of $C_{60}$ is 7 Å.[3,5] An estimate of the usable interior cavity can be obtained by considering the degree to which the electron density of each (equivalent) carbon in the skeletal network penetrates into the interior region. This requires that the effective radius of each carbon be known so that twice this radius can be subtracted from the 7-Å diameter obtained from the X-ray crystal structure.[5] We estimate the radius of each skeletal carbon by using the *covalent* radius of carbon, 0.77 Å,[59] and not the van der Waals radius for an isolated C atom. Subtracting 2 × 0.77 from 7 Å leads to a usable interior cavity diameter of 5.5 Å. Alternatively, the experimentally determined $C_{60}$ bond lengths (1.40 and 1.45 Å)[21] can be halved to estimate the radius of each skeletal carbon, and this also leads to an inner diameter of 5.5 Å. This is approximately the same as the van der Waals diameter of two He atoms, and it is, therefore, not unreasonable that two He atoms can be captured to produce the $C_{60}He_2^{\bullet+}$ product ion.

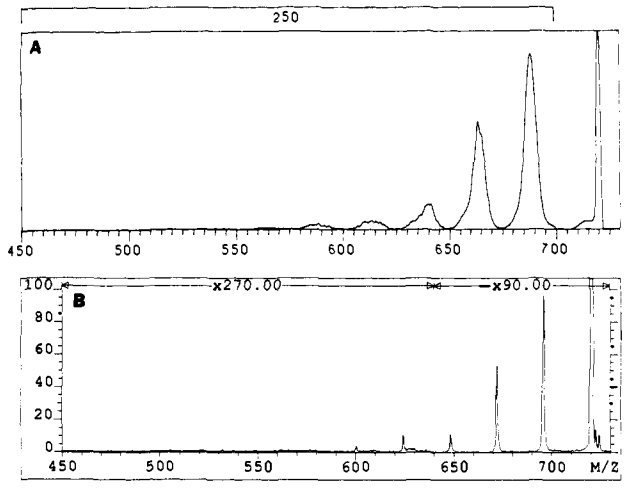


Figure 8. Partial spectrum of product ions resulting from high-energy collisions of $C_{60}^{\bullet+}$ with $D_2$ obtained with the three-sector (A) and the four-sector (B) tandem mass spectrometers. The bump comprising the low-energy tail in (A) is a broad peak and contains the product ions resulting from incorporation of D and $D_2$, loss of D and $D_2$, and elastically scattered ions. The two peaks at $m/z$ 722 and 724 in (B) correspond to $C_{60}D^+$ and $C_{60}D_2^{\bullet+}$, respectively.

The end point of $C_n$ loss for $C_{70}^{\bullet+}$ is difficult to measure because the fullerene product ions of carbon number less than 50 are of very low abundance. These ions already correspond to the formal loss of more than 10 $C_2$ units. The lowest carbon number product ion we detected is $C_{44}^{\bullet+}$.

**2. $D_2$ Collision Gas.** The molecular and atomic weights of $D_2$ and He are very similar, 4.0282 and 4.0026, respectively. Therefore, the center-of-mass collision energy is also very similar. The major differences are that $D_2$ is diatomic and that dissociated $D_2$ is chemically reactive.

**a. Product Ion Spectra.** The high-energy collisions of both $C_{60}^{\bullet+}$ and $C_{70}^{\bullet+}$ with $D_2$ produce a very similar distribution of the all-carbon product ions as for He target gas; the results for $C_{60}^{\bullet+}$ are typical (compare Figures 1A and 2A with Figure 8). The product ions are substantially shifted to kinetic energies lower than those predicted from eq 11. Comparison of the peak widths in the spectra in Figures 1A and 8A reveals that the peaks of the product ions from $D_2$ collisions are singlets. The full width at half-height of the $C_{58}^{\bullet+}/C_{58}He^{\bullet+}$ doublet in Figure 1A is about 120 eV versus 70 eV for $C_{58}^{\bullet+}$ produced from $D_2$ collisions.

**$C_{60}D^+$ and $C_{60}D_2^{\bullet+}$.** Schwarz and co-workers[34a] did not observe $D_2$-containing product ions below $m/z$ 720 for $C_{60}^{\bullet+}$ undergoing high-energy collisions with $D_2$. We also do not detect such product ions. It is possible, however, that single D incorporation does occur, albeit in relatively minor amount. Possible low abundance product ions are seen as shoulders on the high mass side of $C_{54}^{\bullet+}$ through $C_{58}^{\bullet+}$. Nevertheless, we do observe the incorporations of both D and $D_2$ into $C_{60}^{\bullet+}$ (see Figure 8B), phenomena not observed by Schwarz and co-workers.[34a] The direct formation of $C_{60}D^+$ was distinguished from loss of D from $C_{60}D_2^{\bullet+}$ by measuring the kinetic energy of the species produced from each process. Contribution to $C_{60}D^+$ from loss of a single D from $C_{60}D_2^{\bullet+}$ cannot be ruled out and probably does occur.

**b. $C_{60}D_2^{\bullet+}$ and $C_{70}D_2^{\bullet+}$ as the Major Precursor of the Product Ions from $D_2$ Collisions.** As for experiments with He target gas, comparison of the predicted and experimental kinetic energies of the product ions provides insight into the mechanism of the formation of the product ions. We examined the kinetic energies of the $C_{58}^{\bullet+}$ and $C_{56}^{\bullet+}$ product ions and the $C_{68}^{\bullet+}$ and $C_{66}^{\bullet+}$ product ions produced from 8-keV collisions of $C_{60}^{\bullet+}$ and $C_{70}^{\bullet+}$, respectively, with $D_2$. The experimental kinetic energies of these product ions were compared directly to $T_4'$, the kinetic energy

(58) The value of $4E_{cm}$ was obtained by considering the conservation of momentum and energy for collisions when the mass of the target gas is much less than the mass of the projectile ion and there is no internal energy change in the collision partners.

(59) The ionic radii and van der Waals radii were taken from the periodic chart distributed by VCH Publishers, 303 N.W. 12th Ave., Deerfield Beach, FL, 33442-1705.

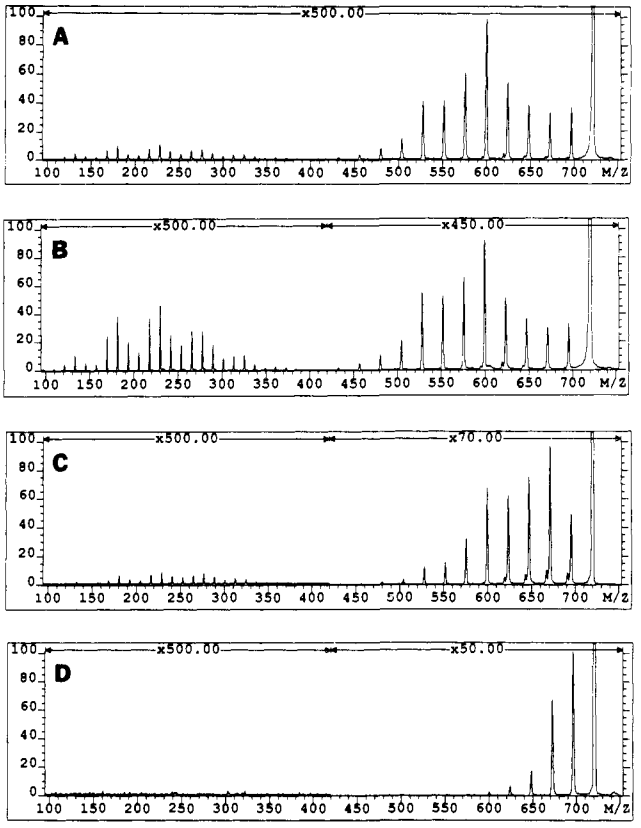


Figure 9. Mass spectra of product ions resulting from high-energy collisions of $C_{60}^{\bullet+}$ with Ne. The collision cell was floated to 0 kV (A), 4 kV (B), 6 kV (C), and 7.2 kV (D). The $C_{60}^{\bullet+}$ precursor ion beam, shown offscale in abundance, was reduced by 50% by the addition of Ne to the collision cell just before each experiment. The $C_{60}Ne^{\bullet+}$ product ion appears as the broadened peak at approximately $m/z$ 740.

derived for product ions that are produced from the intermediate complex between $D_2$ and the fullerene precursor ion. The experimental kinetic energies are nearly equal to $T_4'$ (at 10% beam suppression) but significantly smaller than $T_4$, the kinetic energy of a product ion produced from fragmentation of a fullerene precursor ion that does not contain a $D_2$ molecule. The range of differences between the $T_4'$ and $T_4$ values is 80–90 eV, depending on the system.

The analysis of the kinetic energies of the product ions supports the conclusion that the major precursor ions are the intermediate fullerene endohedral complexes, at least for He and $D_2$ target gases. This mechanism provides an explanation for the shift to low mass (energy) of the product ions as is observed in Figures 1 and 8A. It is possible that the uptake of the center-of-mass collision energy causes the $D_2$ to fragment. The D atoms are subsequently lost (possibly bonded to a departing neutral fragment), and thus few if any endohedral fragments are seen.

**3. Neon Collision Gas. a. Product Ion Spectra.** Spectra of the products of high-energy collisions of both $C_{60}^{\bullet+}$ and $C_{70}^{\bullet+}$ (25% beam suppression) obtained on the three-sector instrument indicate that both of these fullerene molecular ions fragment by apparent loss of consecutive $C_2$ units. A partially resolved doublet is also observed for the single $C_2$ loss product ion in each spectrum. This doublet is especially pronounced for the loss of $C_2$ from $C_{70}^{\bullet+}$. Each component of the doublet is substantially energy shifted, and neither has any significant contribution from the metastable loss.

**b. Low Mass Product Ions.** In comparison to collisions with He and $D_2$, more low mass product ions are produced as a result of collisions with Ne (25% beam suppression). This is probably the result of the increased center-of-mass energy available in the collision with Ne target gas. The low mass ions consist of both even and odd number carbon species (see Figures 9A and 10). Floating the collision cell results in better detection of low mass

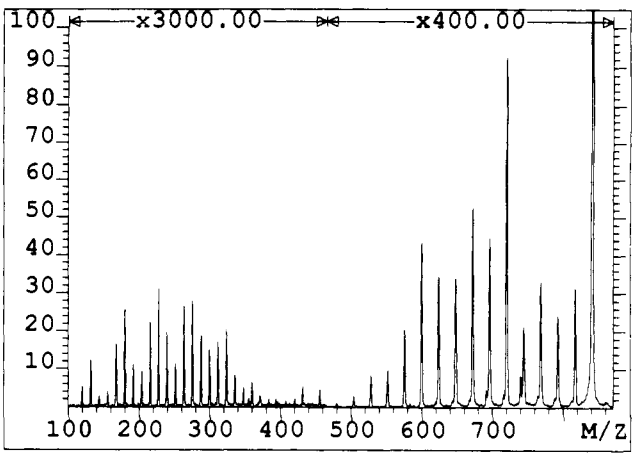


Figure 10. Mass spectrum of product ions resulting from high-energy collisions of $C_{70}^{\bullet+}$ with Ne. The Ne-containing product ions appear as peaks 20 u to higher mass. The $C_{60}Ne^{\bullet+}$ product ion is the most abundant Ne-containing product ion and appears at $m/z$ 740. The $C_{70}Ne^{\bullet+}$ product ion appears as the broadened peak at approximately $m/z$ 860.

product ions, a well-known phenomenon in tandem mass spectrometry. The low mass product ion distribution is most clearly observed in Figure 9B. The increased relative abundances of the $C_{15}^{\bullet+}$, $C_{19}^{\bullet+}$, $C_{22}^{\bullet+}$, and $C_{23}^{\bullet+}$ at $m/z$ 180, 228, 264, and 276 parallel the relative abundances of these low mass species produced from laser vaporization of graphite,[8b,60] as was also noted by Doyle and Ross.[33]

**c. High Mass Product Ions.** For both $C_{60}^{\bullet+}$ and $C_{70}^{\bullet+}$ precursors, the extent of $C_n$ loss is greater for collisions with Ne than with He. The most abundant product ion from $C_{60}^{\bullet+}$ is $C_{50}^{\bullet+}$, which is predicted[4] to have a closed carbon cage. It is also most abundant in the long time scale metastable decay spectrum[45] of $C_{60}^{\bullet+}$. The most abundant product ion from $C_{70}^{\bullet+}$ is $C_{60}^{\bullet+}$, which is also a dominant ion in the long time scale metastable decay spectrum of $C_{66}^{\bullet+}$, $C_{70}^{\bullet+}$, and $C_{74}^{\bullet+}$.[45] The distribution of fullerene product ions below $C_{50}^{\bullet+}$ in Figure 10 is nearly identical to that in Figure 9A. The dominance of the closed-cage fullerenes in the spectrum can be accounted for by considering that these structures are accessed in the higher center-of-mass collision energy experiments with Ne collision gas. These ions are not dominant for collisions with He.

**$C_{60}Ne^{\bullet+}$ and $C_{70}Ne^{\bullet+}$.** We also observed the direct capture of the Ne target gas by $C_{60}^{\bullet+}$ *and* $C_{70}^{\bullet+}$ to produce $C_{60}Ne^{\bullet+}$ and $C_{70}Ne^{\bullet+}$, respectively. As for collisions with He, this is significant evidence for the direct production of another fullerene noble gas endohedral complex. The $C_{60}Ne^{\bullet+}$ ion is even of lower abundance at $T_c$ = 8 keV, when the collision cell is unfloated, Figure 9A. This corresponds to a center-of-mass collision energy of 218 eV, which is incorporated into the internal modes of the $C_{60}Ne^{\bullet+}$ product ion.[61] Because the mass of the neon target is about 5 times the mass of helium, the kinetic energies of the initially formed endohedral complexes as well as the Ne-containing fragments are expected to be even more energy shifted than the He analogues, in accord with eq 10. This may be the reason why the Ne-containing product ions were almost missed by Schwarz and co-workers,[34a] who used an instrument that has a conventional ESA for MS2.

The $C_{60}Ne^{\bullet+}$ ion is of low abundance in all of the spectra in Figure 9, but is most abundant when the collision cell is floated to 7.2 kV. At this collision cell voltage, $T_c$ = 800 eV and $E_{cm}$ = 22 eV. This is the same center-of-mass collision energy in which the $C_{60}He^{\bullet+}$ ion is observed to be most abundant (Figure 5B) and establishes 22 eV as an upper limit for the activation energy to insert Ne into $C_{60}^{\bullet+}$. As for collisions with He, the Ne-containing

(60) Rohlfing, E. A.; Cox, D. M.; Kaldor, A. *J. Chem. Phys.* **1984**, *81*, 3322.

(61) This value for $E_{cm}$ was obtained by using the average molecular weight for $m_N$ in eq 18.

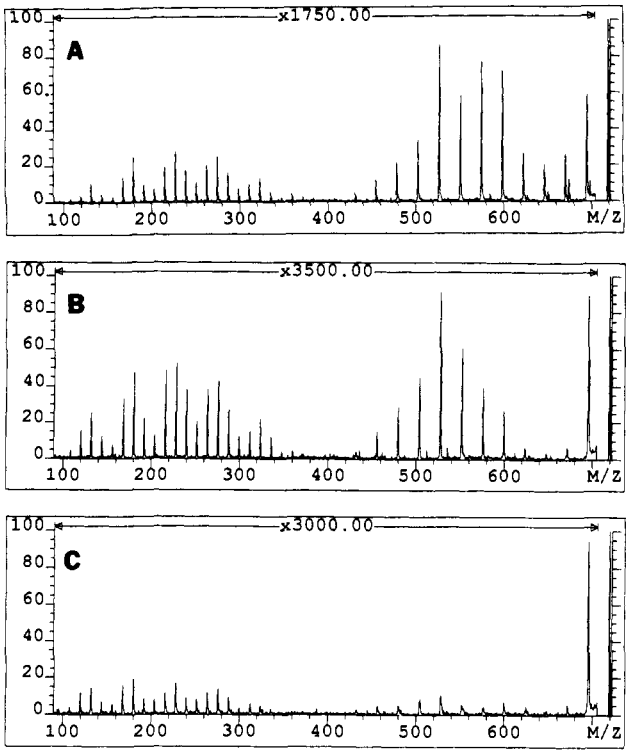


Figure 11. Mass spectra of product ions resulting from high-energy collisions of 8-keV $C_{60}^{\bullet+}$ with Ar (A), Kr (B), and Xe (C) collision gas. A beam suppression of 50% was used for each experiment.

product ions, $m/z$ 572, 596, 620, 644, 668, and 692, increase in relative abundance as the collision cell is floated and the internal energy of the $C_{60}Ne^{\bullet+}$ ion is decreased. Again, this is expected for product ions formed via mechanism 1 in Scheme I. Not surprisingly, the most abundant Ne-containing product ion from $C_{70}^{\bullet+}$ is $C_{60}Ne^{\bullet+}$. Theoretical calculations pertaining to neutral $C_{60}Ne$ indicate that $C_{60}Ne$ is essentially at the same energy as the separated components.[51]

**d. End Point of $C_n$ Loss.** Amplification of the spectrum in Figure 9A reveals that $C_{32}^{\bullet+}$ is the end point for production of even-carbon product ions. This same end point was observed in photofragmentation studies of $C_{60}^{\bullet+}$.[45] Although $C_{32}^{\bullet+}$ is detected above the noise, it is the least abundant product ion. Below $C_{32}^{\bullet+}$, both even and odd carbon number product ions are clearly observed beginning with $C_{31}^{\bullet+}$. The end point for $C_n$ loss from $C_{70}^{\bullet+}$ appears to be $C_{38}^{\bullet+}$.

It is of interest to compare the end point of equivalent $C_n$ loss from $C_{60}Ne^{\bullet+}$ with the results for metal ion containing fullerenes. The van der Waals radius of Ne is 1.5 Å, which is intermediate between the radius of the metal ions $K^+$ (1.4 Å) and $Cs^+$ (1.7 Å). The lowest carbon number Ne-containing product ion we observe is possibly $C_{44}Ne^{\bullet+}$, but unambiguously $C_{46}Ne^{\bullet+}$. The $C_{46}Ne^{\bullet+}$ product ion is intermediate between $C_{44}K^+$ and $C_{48}Cs^+$, the lowest carbon number fullerenes containing these metals. The diameter of two Ne atoms is 6 Å. This is less than the 7-Å diameter of $C_{60}$ obtained from X-ray crystallography, but more than the estimated usable inner diameter of 5.5 Å; the species $C_{60}Ne_2^{\bullet+}$ is not detected as a product of collisions of $C_{70}^{\bullet+}$ with Ne.

**4. Argon, Krypton, and Xenon Collision Gas.**[62] **a. Product Ion Spectra.** We examined the collisional activation of 8-keV $C_{60}^{\bullet+}$ with the remainder of the noble gases and of 8-keV $C_{70}^{\bullet+}$ with argon. Only collisions of $C_{60}^{\bullet+}$ with argon produce product ions containing the target gas, which are easily observed at $m/z$ 700, 676, 652, and 628 in Figure 11. Unlike the series of He and Ne incorporation product ions, this ion series consists of $C_{55}Ar^{\bullet+}$, $C_{53}Ar^{\bullet+}$, $C_{51}Ar^{\bullet+}$, and $C_{49}Ar^{\bullet+}$, all *odd*-carbon species presumably formed from the loss of neutral $C_5$, $C_7$, $C_9$, and $C_{11}$ from (transient) $C_{60}Ar^{\bullet+}$. The loss of odd-carbon neutrals is intriguing because these are the losses expected on the basis of the thermodynamic stability of the neutrals lost. An unsolved puzzle has been why the fullerenes photofragment by loss of the elements of even-carbon neutrals,[45] which is also observed in collisional activation.[29,32-34a] Perhaps the activation barrier for the favored odd-carbon losses can be surmounted as a result of the large internal energy (421 eV) deposited into the transient $C_{60}Ar^{\bullet+}$ ion as a result of Ar capture.

(62) The major isotopes of these noble gases are $^{40}Ar$ (99.6%), $^{84}Kr$ (56.9%), $^{129}Xe$ (26.4%), and $^{132}Xe$ (26.9%).

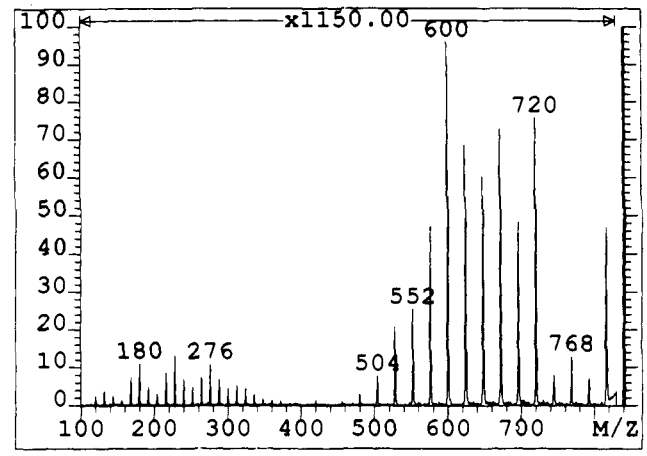


Figure 12. Partial mass spectrum of product ions resulting from high-energy collisions of $C_{70}^{\bullet+}$ with Ar (50% beam suppression). The closed-cage fullerene product ions $C_{50}^{\bullet+}$ and $C_{60}^{\bullet+}$ appear at $m/z$ 600 and 720, respectively.

As pointed out in the discussion of He and Ne target gases, the energy shift of the product ions containing target gas depends on the mass of the target gas. For $C_{55}Ar^{\bullet+}$ formed from $C_{60}Ar^{\bullet+}$, the difference between the expected ion energy and that predicted from eq 10 is

$$T_{exp} - T_{3,CW} \cong 800 \text{ eV} \quad (20)$$

The $C_{55}Ar^{\bullet+}$ is accepted by the second ESA of the four-sector mass spectrometer used here; however, the large shift in the expected kinetic energy would be an overwhelming challenge for an MS2 with a conventional ESA.

The bottlenecks in the fragmentation of $C_{70}^{\bullet+}$ undergoing collisions with Ar are $C_{50}^{\bullet+}$ and $C_{60}^{\bullet+}$ (see Figure 12). The higher carbon fullerene product ions above $C_{60}^{\bullet+}$ are of conspicuously low abundance, and $C_{50}^{\bullet+}$ is the dominant product ion. Because the center-of-mass collision energy is higher with Ar collision gas than with Ne or especially He, more abundant low mass product ions are produced upon collisions with Ar. The distribution of these low mass ions is qualitatively the same as those from $C_{60}^{\bullet+}$. No Ar-containing product ions were detected in the product ion spectrum of $C_{70}^{\bullet+}$ with Ar.

Several trends apparent in the spectra in Figure 11 can be understood by considering the center-of-mass collision energy available for each collision gas: 421, 835, and 1230 eV for Ar, Kr, and Xe, respectively[61] at 8 keV of energy for $C_{60}^{\bullet+}$. The most obvious trend is that the number of product ions detected decreases as the mass of the target gas increases, as indicated by the gain factors. This effect was mentioned in the He discussion and is due, at least in part, to more product ions being scattered to angles beyond the acceptance angle of MS2 as the mass of the target gas is increased.

Another trend, which is the continuation of that observed for collisions with He and Ne, is that the distribution of high mass fullerene product ions shifts to lower carbon number as the center-of-mass collision energy is increased. For example, $C_{50}^{\bullet+}$ is the most abundant product ion formed upon collisions of $C_{60}^{\bullet+}$ with Ne whereas $C_{44}^{\bullet+}$ is the most abundant with Ar. The reduced abundances of $C_{58}^{\bullet+}$, $C_{56}^{\bullet+}$, $C_{54}^{\bullet+}$, and $C_{52}^{\bullet+}$ in Figure 11A suggest that the collisionally activated $C_{60}^{\bullet+}$ precursor ions continue to fragment until the relatively stable $C_{50}^{\bullet+}$ is reached. The higher mass fullerene neighbors of $C_{50}^{\bullet+}$ are even of lower relative abundance in collisions of $C_{60}^{\bullet+}$ with Kr.

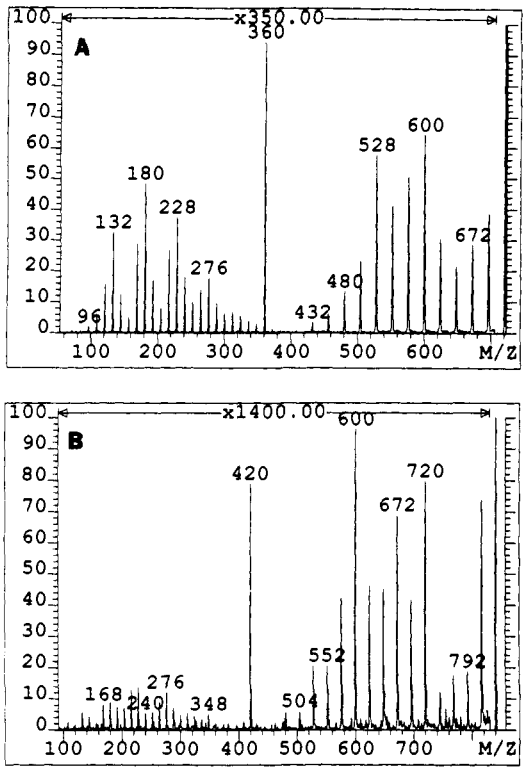


Figure 13. Partial mass spectra of product ions resulting from high-energy collisions of $C_{60}^{\bullet+}$ (A) and $C_{70}^{\bullet+}$ (B) with $O_2$ collision gas. The abundance of the doubly charged $m/z$ 360 ion is enhanced by a factor of 400 by using $O_2$ instead of He as a collision gas.

Collisions of $C_{60}^{\bullet+}$ with xenon produce a low abundance of product ions. The relative abundance of $C_{58}^{\bullet+}$ produced from $C_2$ loss may be enhanced by residual $C_{58}^{\bullet+}$ from unimolecular decay. This may be why the abundance of $C_{58}^{\bullet+}$ is comparable in all of the spectra in Figure 11.

**b. End Point of $C_n$ Loss for Ar Target Gas.** The lowest even-carbon product ion produced upon collisions of $C_{60}^{\bullet+}$ with Ar is $C_{32}^{\bullet+}$, the same as that for Ne collision gas. The lowest even-carbon product ion for $C_{70}^{\bullet+}$ undergoing collisions with Ar is $C_{36}^{\bullet+}$ or possibly $C_{34}^{\bullet+}$. The increased relative abundance of $m/z$ 420 is probably not due to $C_{35}^{\bullet+}$, but to $C_{70}^{2+}$. The lowest carbon number Ar-containing product ion appears to be $C_{49}Ar^{\bullet+}$, which given the similarity in van der Waal radii of Ar and $Cs^+$, compares well with the $C_{48}Cs^+$ end point.[50]

**c. Translational Energy Loss Measurements.** The kinetic energies of the product ions resulting from collisions of 8-keV $C_{60}$ radical cations with xenon are more conventional than the results for small collision gases, presumably because the Xe target gas is not captured owing to the high center-of-mass collision energy and the size of the Xe atom. The $C_{58}^{\bullet+}$ fragment ion produced from $C_{60}^{\bullet+}$ with Xe collision gas is an apparent singlet. The peak width at half-height is 52 eV, which is broadened somewhat from the collisional activation process because the half-height width of $C_{58}^{\bullet+}$ from metastable decomposition is 31 eV. This half-height width of 52 eV is less than that of $C_{58}^{\bullet+}$ (70 eV) produced from $D_2$ collisions, because the peak has not been further broadened by loss of the incorporated $D_2$.

For product ions resulting from collisions, a small peak shift to lower energy is expected because an energy decrement must occur to drive the $C_{60}^{\bullet+}$ fragmentation chemistry. A $\Delta T$ value of 12.2 ± 1 eV is associated with production of $C_{58}^{\bullet+}$. This energy represents an upper limit of the energy required to remove $C_2$ from $C_{60}^{\bullet+}$ and agrees within experimental error with the value 12.8 eV obtained from laser photofragmentation studies.[45]

The translational energy loss, $\Delta T$, for $C_{56}^{\bullet+}$ produced from $C_{60}^{\bullet+}$ is 32 ± 1 eV, an upper limit for the energy required to remove the elements of $C_4$. The energy is more than twice that required to remove $C_2$, suggesting that $C_4$ is removed in two steps.

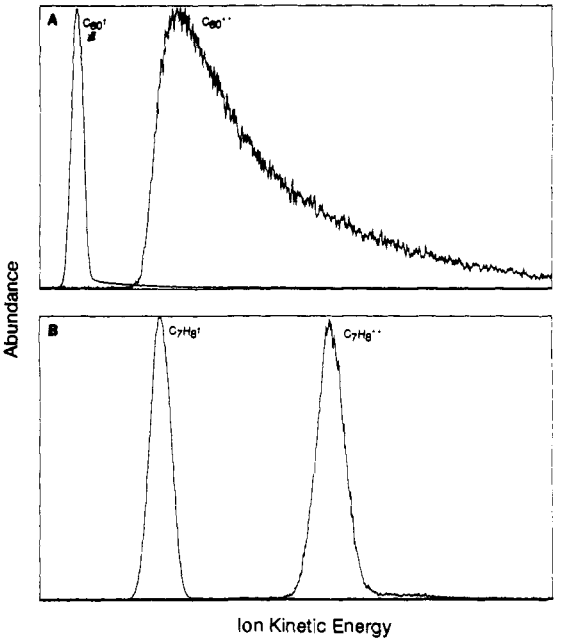


Figure 14. (A) Kinetic energy profile of $C_{60}^{2+}$ overlayed with the profile of the $C_{60}^{\bullet+}$ precursor ion. The sweep width was 10 000 ppm. (B) Kinetic energy profile $C_7H_8^{2+}$ overlayed with the profile of the $C_7H_8^{\bullet+}$ precursor ion. The sweep width was 6000 ppm, and for (A) and (B) the scan is from high to low kinetic energy (left to right). The data presented are the raw, unsmoothed data.

**5. $N_2$, NO, and $O_2$ Collision Gas. a. Product Ion Spectra.** The product ion spectra obtained with $N_2$, NO, or $O_2$ are qualitatively similar to those obtained by using Ar collision gas, with the exception that the former gases lead to dramatically enhanced abundances of doubly charged molecular ions[63] and that $N_2$- or $O_2$-containing product ions are not detected. The order of the doubly charged ion enhancement by the collision gases is $O_2$ > NO > $N_2$ (see Figure 13 for the $C_{60}^{\bullet+}$ and $C_{70}^{\bullet+}$ $O_2$ CAD spectra). For $C_{60}^{\bullet+}$, the doubly charged molecular ion is the most abundant product ion, and for $C_{70}^{\bullet+}$ it is greatly enhanced. Some aspects of high-energy collisions of $C_{60}^{\bullet+}$ with $O_2$ were discussed previously.[33]

The process of removing an electron from a precursor ion is known as charge stripping. Charge stripping of doubly charged fullerene ions, produced directly by electron ionization, gives abundant triply charged ions.[26,33,44] The large relative abundance of the doubly and triply charged fullerenes is surely related to the ability of these highly aromatic species to disperse the charges over a large area.

**b. Charge Stripping and the Second Ionization Energies of $C_{60}$, $C_{70}$, and $C_{84}$.** As is discussed in the Experimental Section, measurement of the $\Delta T$ of the charge-stripping peak gives a measure of the second ionization energy of the neutral species.[37,38] The basic premise is that the energy to remove the electron comes from the kinetic energy of the precursor ion. The apparent second ionization energies of $C_{60}$, $C_{70}$, and $C_{84}$ are 11.9, 12.0, and 12.0 ± 0.5 eV, respectively. These values are lower but within experimental error of the values reported recently by Lifshitz and co-workers.[26] The second ionization energies of $C_{60}$ obtained by the charge-stripping method do not agree with the value 9.7 eV obtained by charge-transfer bracketing,[25] but are close to 11.2 eV, a recently calculated value.[64]

The method used here to measure the second ionization energy does not require that an external standard be used. A common standard used in other procedures is toluene, which has an accepted value of 15.7 ± 0.2 eV[65] for the second ionization energy. To verify

(63) These results were presented by M. L. Gross at the American Society for Mass Spectrometry Sanibel Island Conference on Ion Activation and Dissociation, January 29, 1991, and at the 201st National ACS meeting, Atlanta, GA, April 15, 1991.

(64) Gallup, G. A. *Chem. Phys. Lett.* **1991**, *187*, 187.

the method used in this study, we measured the toluene second ionization energy, and the value obtained was 15.2 eV which is 0.5 eV lower than the value 15.7 eV extracted from the ionization efficiency curve of doubly charged toluene.[65]

The peak shape of the doubly charged fullerene ions reveals a strong tail to lower energy, especially when compared to that for toluene (see Figure 14). The shape of the $C_{60}^{2+}$ charge-stripping peak for $O_2$ resembles those of the other collision gases. This degree of tailing is not commonly observed in charge-stripping peaks of smaller organic cations.[37,38] There are two probable explanations. The ion population of the low-energy tail consists of those ions that have lost additional kinetic energy by transfer of momentum to the $O_2$ collision gas, analogous to the results discussed for He, implying that nearly direct collisions are occurring in the charge-stripping process. Alternatively, the ion population of the low-energy tail consists of those doubly charged ions that have converted some kinetic energy, in addition to that used to remove the electron, into internal energy of the doubly charged ion. One mechanism for exciting the doubly charged ion is by removal of low-lying electrons, which may be a facile process owing to the unusual electronic structure of the fullerenes. Doubly charged ions that form in a collision to give internally excited target gas would also appear in the low-energy tail.

## Conclusion and Summary

Both a three-sector and a four-sector mass spectrometer were used to study the products of high-energy collisions of fullerene molecular ions with various target gases. Small target gases are captured directly, and the various endohedral complexes are observed as product ions. Evidence for capture of Ar is indirect owing to the high internal energy of the Ar endohedral complex formed by high-energy collisions. Analysis of the kinetic energies of the product ions produced from He and $D_2$ collisions leads to the conclusion that the endohedral complex fragments to produce the observed product ions. Charge stripping of the fullerene precursor ions leads to the production of abundant doubly charged molecular ions, and this allowed the apparent second ionization energy of $C_{60}$, $C_{70}$, and $C_{84}$ to be measured.

Reasonable conclusions can now be drawn about mechanistic details. For example, the direct loss of an intact $C_{10}$ unit from $C_{70}He^{\bullet+}$ to produce $C_{60}He^{\bullet+}$ should open a hole in the carbon cage and allow the He atom to escape. If the $C_{60}He^{\bullet+}$ species, however, were formed by consecutive $C_2$ losses from $C_{70}He^{\bullet+}$, then the carbon cage could anneal, preventing He escape.

For $C_{60}He^{\bullet+}$, the end point of $C_n$ loss is $C_{44}He^{\bullet+}$. It is difficult to accept that the direct loss of a $C_{16}$ molecule would not allow release of the entrapped He. The bond lengths for $C_{60}$ are 1.4 and 1.45 Å,[21] which are approximately half the van der Waals diameter of He, in line with this simple argument for consecutive $C_2$ loss from $C_{60}He^{\bullet+}$. Unpublished results of a theoretical calculation[66] also support a consecutive $C_2$ loss mechanism.

High-energy collisional activation and MS/MS should prove to be an effective tool for qualitative analysis of other fullerenes, fullerene analogues, and fullerene-based materials. A test for the presence of a closed-cage structure is capture of a He atom or other noble gas atoms. If the product ions containing He are considered interferences, then $N_2$ or $O_2$ should be used as a collision gas.

**Acknowledgment.** We are grateful to Robert Bateman of VG Analytical (Fisons Instruments) who designed the four-sector tandem mass spectrometer used in this work and who advised us on experimental aspects of this work. K.A.C. expresses sincere appreciation to Don Rempel for the informative late-night chalkboard discussions of electrostatic analyzers and their aberrations, and the energetics associated with various fragmentation pathways. The research was supported by the National Science Foundation (Grant No. CHE 9017250).

(65) Dorman, F. H.; Morrison, J. D. *J. Chem. Phys.* **1961**, *35*, 575.

(66) Reference 13 in ref 42 of this paper.

# Solid-State Reactions Studied by Carbon-13 Rotor-Synchronized Magic Angle Spinning Two-Dimensional Exchange NMR. 1. Self-Diffusion and the Tautomeric Hydrogen Shift in Tropolone

**Jeremy J. Titman, Zeev Luz,† and Hans W. Spiess***

*Contribution from the Max-Planck-Institut für Polymerforschung, Postfach 3148, D-6500 Mainz, Germany.* *Received November 12, 1991*

**Abstract:** Two-dimensional carbon-13 magic angle spinning exchange NMR experiments with rotor-synchronized mixing times have been carried out for solid tropolone at 40 °C and at variable spinning frequencies. At low spinning rates, a complicated spectrum is obtained with cross peaks linking different sidebands of the same carbon atom ("auto" cross peaks) as well as ones linking sidebands of chemically different atoms that are exchanged by a tautomeric hydrogen shift process ("hetero" cross peaks). The results are interpreted in terms of a translational diffusion mechanism in which tropolone molecules undergo lattice jumps between different sites. To retain the crystal order, certain lattice jumps require that the molecules undergo a concomitant hydrogen shift and/or a $\pi$-flip about an axis in the molecular plane. From the results, a self-diffusion constant of $D \cong 4 \times 10^{-21}$ m$^2$ s$^{-1}$ is estimated for solid tropolone at room temperature.

## Introduction

Tropolone is one of a family of $\alpha$-hydroxy ketones which undergo a tautomeric hydrogen shift reaction. In solution the proton and carbon-13 NMR spectra always exhibit averaged signals due to the two tautomeric forms from which a lower limit of $10^8$ s$^{-1}$ can be set for the rate of the hydrogen shift at room temperature.[1,2]


† Permanent address: The Weizmann Institute of Science, Rehovot 76100, Israel.

0002-7863/92/1514-3756$03.00/0 